8-2015

Feasibility of Using Virtual Unenhanced Images to Replace Pre-contrast Images in Multiphase Renal CT Examinations

Dawn Olivia Popnoe

FEASIBILITY OF USING VIRTUAL UNENHANCED IMAGES TO REPLACE PRE-CONTRAST IMAGES IN MULTIPHASE RENAL CT EXAMINATIONS

By

Dawn Olivia Popnoe, B.S.

APPROVED:

_____

Kyle Jones, Ph.D., Advisory Professor

_____

Dianna Cody, Ph.D.

_____

Cheenu Kappadath, Ph.D.

_____

Tinsu Pan, Ph.D.

_____

Shouhao Zhou, Ph.D.

APPROVED:

_____

Dean, The University of Texas

Graduate School of Biomedical Sciences at Houston

FEASIBILITY OF USING VIRTUAL UNENHANCED IMAGES TO REPLACE PRE-

CONTRAST IMAGES IN MULTIPHASE RENAL CT EXAMINATIONS

A

THESIS

Presented to the Faculty of

The University of Texas

Health Science Center at Houston

and

The University of Texas

M.D. Anderson Cancer Center

Graduate School of Biomedical Sciences

in Partial Fulfillment

of the Requirements

for the Degree of

MASTER OF SCIENCE

By

Dawn Olivia Popnoe, B.S.

Houston, Texas

August, 2015

Dedication

To Haden, you are the best and I can't thank you enough for always being there for me.

I love you.

Acknowledgements

FEASIBILITY OF USING VIRTUAL UNENHANCED IMAGES TO REPLACE PRE-CONTRAST IMAGES IN MULTIPHASE RENAL CT EXAMINATIONS

Dawn Olivia Popnoe, B.S.

Advisory Professor: Kyle Jones, Ph.D.

Multiphase renal CT exams are a commonly used imaging technique for the diagnosis of renal masses. The pre-contrast, or true unenhanced (TUE), image provides a baseline for enhancement measurements which is an important criteria used to characterize renal lesions, consequently it is crucial that CT numbers measured in TUE images be accurate. The purpose of this work is to assess the feasibility of replacing TUE with virtual unenhanced (VUE) images derived from DECT data in renal CT exams. Eliminating TUE image acquisition would reduce patient dose and increase patient throughput, improving clinical efficiency.

A retrospective study was conducted for 60 consecutively selected patient exams. VUE and TUE images were compared qualitatively and the differences were tested using a Bayesian Hierarchical model. VUE images were found to be inferior to TUE images for visualization of major vessels and depiction of liver parenchyma. CT numbers were measured in the liver, spleen, spine, aorta, cystic lesions, subcutaneous fat, renal cortex and medulla, and the differences were tested with a Student's paired t-test. There were significant differences between TUE and VUE measurements (p-value > 0.05) in the spleen, spine, aorta, renal cortex, subcutaneous fat, and inferior vena cava. However, evaluation of the clinical relevance based on grayscale perceptibly indicated that the difference for the spleen and subcutaneous fat are not clinically meaningful.

The rapid kVp-switching GE CT750HD scanner was used to assess enhancement accuracy when using VUE compare to TUE images as the baseline for enhancement calculations

across a wide range of clinical scenarios simulated in a phantom study, and the results were analyzed using Bayesian Hierarchical models. For simulation of angiomyolipoma and benign cystic lesions, enhancement values were not significantly different. However, for simulation of Bosniak category II-IV lesions, differences in measured enhancement were found to be significant. Additionally, the effect of ASIR level used in image reconstruction was assessed, and found not to affect measured CT number using a mixed effects model.

Differences in measured enhancement values for simulated borderline enhancing renal lesions demonstrate that replacement of TUE with VUE images is not feasible with the current iteration of the algorithm.

Table of Contents

List of Illustrations

List of Tables

List of Abbreviations

AML   Angiomyolipoma

ASIR   Adaptive Statistical Iterative Reconstruction

CI   Confidence Interval

cRCC   Clear Cell Renal Carcinoma

CT   Computed Tomography

CTDI   Computed Tomography Dose Index

DE   Dual Energy

DECT   Dual Energy Computed Tomography

DFOV   Display Field of View

FOV   Field of View

GSI   Gemstone Spectral Imaging

HDPE   High Density Polyethylene

HU   Hounsfield Unit

kVp   Peak Kilovoltage

MSI   Material Suppressed Iodine

pRCC   Papillary Renal Cell Carcinoma

RCC   Renal Cell Carcinoma

ROI   Region of Interest

SD   Standard Deviation

SDOM   Standard Deviation of the Mean

SECT   Single Energy Computed Tomography

SFOV	Scanning Field of View
SE	Standard Error
TUE	True Unenhanced
VUE	Virtual Unenhanced
WW/WL	Window width/Window level

Chapter 1. Introduction and Background

1.1 Computed Tomography

Computed Tomography (CT) is a commonly used imaging technique in volumetric dataset of the patient anatomy is acquired and reconstructed to provide a three-dimensional representation of the linear attenuation coefficients contained within each voxel in the field of view (FOV). This imaging modality provides a non-invasive method for patient diagnosis, and is performed annually around 70 – 80 million times in the United States [1]. First introduced in clinical practice in 1972, CT has since revolutionized both medical imaging and the practice of medicine [2].

1.1.1 Single Energy Computed Tomography

Single Energy Computed Tomography (SECT), commonly referred to as conventional CT, is based on the fact that each material within the CT field of view (FOV) has a characteristic linear attenuation curve, which in turn dictates the ways in which each material interacts with an X-ray beam. CT images are reconstructed from line integral measurements of X-ray attenuation through the human body using mathematical concepts first discussed by Johann Radon in 1917 [2].

The primary modes for X-ray interaction in the energy range used for diagnostic CT imaging are the photoelectric effect and incoherent (Compton) scattering. The photoelectric effect occurs when an incident X-ray photon transfers all of its energy to an inner shell atomic electron, which is then ejected from the atom. The probability of this interaction is approximately proportional to the atomic number cubed and inversely proportional the energy cubed [1]. This energy dependence, in conjunction with differences in K absorption edges of different atomic elements, is a fundamental concept facilitating the dual energy technique [3]. Incoherent scattering refers to the interaction of an incident photon with a valence electron, where the

electron is ejected from the atom, and the photon is scattered with a fraction of its initial energy. This is the predominant interaction mechanism in the diagnostic energy range above 26 keV [1]. In contrast to the photoelectric effect, Compton scatter is almost independent of photon energy, and instead is strongly dependent on the electron density of a material.

An X-ray source that is contained within the CT scanner produces a spectrum of X-rays with a peak kilovoltage (kVp) typically ranging between 80 – 140, and a corresponding array of detectors is aligned opposite of the X-ray source [1]. During data acquisition, the X-ray source and detector array rotate synchronously around the axis of the gantry. Originally, CT images were acquired with axial scanning, which involves the translation of the object to be imaged along the z-axis of the scanner between sequential cycles of the gantry, resulting in the reconstruction of one or more images per rotation, depending on the number of detector rows. Helical CT defines a mode of operation in which the object to be imaged is translated along the z-axis while the X-ray source is rotating, resulting in the volumetric set of line integrals of attenuation through the object. Interpolation is then used to produce sets of coplanar projections from the three-dimensional data set which are then reconstructed into image sets using filtered back projection or iterative reconstruction [4]. In either case, the images produced are attenuation maps of the materials and tissues contained within the field of view (FOV), each having a characteristic linear attenuation coefficient, μ, which is dependent on photon energy and therefore kV and beam filtration [5]. The image is comprised of an array of voxels, each with a gray scale value based on the X-ray attenuation within that voxel. The gray scale value is referred to as a Hounsfield Unit (HU) and is defined as [1]:

$$HU(x, y, z) = 1000 * \left(\frac{\mu(x,y,z) - \mu_w}{\mu_w} \right)$$
Equation 1.1.1-1

where $\mu(x,y,z)$ is the average linear attenuation coefficient measured in a voxel located at (x,y,z) within the patient and μ_w is the linear attenuation coefficient of water. This provides a relative attenuation measurement in which the attenuation is scaled to that of water (HU=0).

1.1.2 Dual Energy Computed Tomography

Dual Energy Computed Tomography (DECT) is an extension of SECT in which two data sets are acquired using different X-ray energy spectra. DECT was originally proposed in the late 1970s, but technical limitations of early CT scanners limited the success of the technique [1, 6-9]. DECT was abandoned because the acquisition times of early scanners were long and two consecutive scans were needed which led to motion misregistration between data sets, as well as additional radiation exposure [9]. With the advanced capabilities of newer scanners, there has been renewed interest in the clinical use of DECT. One potential benefit of this technique is that it can provide information regarding the material composition within each voxel by exploiting attenuation variations of photon absorption at different energies as well as attenuation differences of materials with high atomic numbers [9]. In addition to enhancing material differentiation, DECT has the potential to reduce beam hardening artifacts [8].

DECT has the potential to expand the capabilities of CT by allowing for the estimation of the linear attenuation curve for each voxel in the object, providing both spatial and material information, as opposed to only a spatial map of scalar HU values [10]. This is accomplished by measuring the attenuation of materials in the FOV using two different effective X-ray energies and then extrapolating, using knowledge of the exponential behavior of X-ray attenuation of materials, to estimate the full attenuation curve. This curve can then be compared to known attenuation curves to gain information as to composition of the material.

The foundation of this material decomposition technique exploits the fact that the attenuation coefficient for a given material is a function of a unique combination of photoelectric and incoherent scattering probabilities, which are related to effective atomic number and electron

3

density, respectively. For a given material, the attenuation coefficient as a function of energy μ(E) may then be represented as a unique combination of photoelectric and incoherent scatter coefficients:

$$\mu(E) = \alpha f_{PE} + \beta f_C \qquad \text{Equation 1.1.2-1}$$

where f_{PE} represents the photoelectric dependence, which depends strongly on atomic number and therefore provides information as to the composition of the object, and f_C represents the Compton scatter coefficient, which depends strongly on electron density and is therefore proportional to mass density [11]. The weighted linear combination of these two coefficients can represent the mass attenuation coefficient of any material in the diagnostic energy range [12]. However, discontinuities at the K-edge of a material can complicate the simplified assumption that this is a linear combination. Consider as an example iodine, which is commonly used as a contrast agent in diagnostic imaging due to its 33.2 keV K-edge. If the effective energy of the beam is just above this K-edge, the probability of photoelectric interaction (f_{PE}) will be approximately six times greater than the probability for energies just below the K-edge, 33.1 keV [1].

Following on this technique, a basis pair of two materials may be chosen, such that all materials contained within a given voxel in a DECT image are assumed to be a weighted combination of the selected basis pair, e.g., water and iodine. Note that it is crucial that the selected materials differ substantially in atomic number and electron density so that they consequently differ in photoelectric and incoherent scatter attenuation cross sections, resulting in a large separation between the linear attenuation curves. The total linear attenuation coefficient in any voxel can be expressed as a weighted combination of the attenuation of basis materials 1 and 2:

$$\mu(E) = \delta_1 * \mu_1(E) + \delta_2 * \mu_2(E) \qquad \text{Equation 1.1.2-2}$$

where

$$\mu_1(E) = \alpha_1 f_{PE} + \beta_1 f_C \quad and \quad \mu_2(E) = \alpha_2 f_{PE} + \beta_2 f_C \qquad \text{Equation 1.1.2-3}$$

In Equation 1.1.2-2 the variable δ_i represents the weighting of the corresponding basis material such that the combination of weighted attenuation from each material in the basis pair yields the measured attenuation of the material in the voxel. The system of equations given in Equation 1.1.2-3 can be solved for f_{PE} and f_C:

$$f_{PE} = \frac{\mu_2 \beta_1 - \mu_1 \beta_2}{\alpha_2 \beta_1 - \alpha_1 \beta_2} \qquad \text{Equation 1.1.2-4}$$

$$f_C = \frac{\mu_2 \alpha_1 - \mu_1 \alpha_2}{\alpha_1 \beta_2 - \alpha_2 \beta_1} \qquad \text{Equation 1.1.2-5}$$

Substituting Equations 1.1.2-4 and 1.1.2-5 into Equation 1.1.2-3 followed by 1.1.2-2 and then rearranging yields:

$$\mu(E) = \delta_1 \left[\alpha_1 \left(\frac{\mu_2 \beta_1 - \mu_1 \beta_2}{\alpha_2 \beta_1 - \alpha_1 \beta_2} \right) + \beta_1 \left(\frac{\mu_2 \alpha_1 - \mu_1 \alpha_2}{\alpha_1 \beta_2 - \alpha_2 \beta_1} \right) \right] + \delta_2 \left[\alpha_2 \left(\frac{\mu_2 \beta_1 - \mu_1 \beta_2}{\alpha_2 \beta_1 - \alpha_1 \beta_2} \right) + \beta_2 \left(\frac{\mu_2 \alpha_1 - \mu_1 \alpha_2}{\alpha_1 \beta_2 - \alpha_2 \beta_1} \right) \right]$$

Equation 1.1.2-6

Equation 1.1.2-6 represents the attenuation coefficient for any material as a weighted combination of the selected basis pair. All subscripts 1 correspond to attenuation properties of the first basis material, and subscripts 2 correspond to the second basis material. Attenuation data can then be measured at two different effective X-ray energies, resulting in two equations (equation 1.1.2-6 at the high and low energy), μ_L and μ_H, with two unknowns, δ_1 and δ_2. Each unknown variable, δ_i, represents the fraction of the material within the voxel attributed to each of the basis materials. Line integrals can then be taken over the linear attenuation coefficient for each ray of each projection and corresponding detector element and used to make measurements of the function being reconstructed to generate an image [11]. The resulting intensity equations can then be solved for δ_1 and δ_2, which are the weightings that combine to yield the unique attenuation of the material in the voxel. An example of material decomposition with a basis pair of water and iodine

for a voxel containing bone is shown in Figure 1. The light blue line indicates the estimated

weighted combination of water and iodine attenuation coefficients, as described.
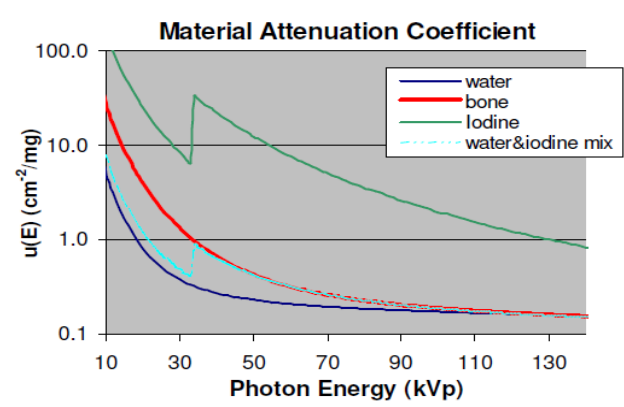
Figure 1. Bone material attenuation coefficient represented as a weighted combination of

water and iodine attenuation coefficients [13]

There are two commonly used techniques for DECT data acquisition. The first is a dual-

source technique that involves the use of two X-ray sources mounted nearly 90^0 apart, a concept

that was first proposed only a few years after CT was first introduced into clinical practice and

then re-introduced in 2006 [7]. A benefit of this technique is that the tube current (mA) can be

selected independently for each X-ray source, which ensures similar X-ray fluence at both beam

energies. This system also offers the potential for increased separation between the two energy

spectra by filtering the high energy X-ray source which increases the contrast between two

materials and therefore improves the performance of DECT algorithms [7]. Disadvantages of this

technique include a limited DECT scan field of view (SFOV) resulting from the smaller coverage

of the second detector array and cross scatter between non-corresponding orthogonal detector

rows [7]. Additionally, the angular separation of the X-ray sources results in a temporal

difference on the order of 100 milliseconds between the high and low energy projections, which

can introduce artifacts from patient motion and result in mis-registration of the two data sets [7].

The second technique currently used for commercial DECT data acquisition involves a

single X-ray source with fast kVp switching. For this technique, the high voltage generator

alternates between high and low kVp at each projection angle, creating an interleaved set of high and low energy projections. The nearly simultaneous acquisition of the two data sets results in better temporal registration, which reduces the potential for motion artifacts while still using the entire SFOV for DECT [8]. Fast switching between two kVps does have technical challenges, including the rise and fall times of the high voltage waveforms, which complicates the determination of the effective energy for the high and low kVp projections [14]. Because this rise and fall of the waveforms occurs during data acquisition, it reduces the achievable separation between the energy spectra [7]. Another consequence of this technique, which uses a single detector array, is that the view integration time is limited by the primary decay of the detector and afterglow performance [8]. The Gemstone scintillator (General Electric Healthcare, Milwaukee, WI) has been developed to minimize this integration time limitation, as it has a decay time of 30 ns which is 100 times faster than the more commonly used gadolinium oxysulfide (Gd_2O_2S) and afterglow levels that reach only 25% of gadolinium oxysulfide [8]. Energy separation is further limited by the use of a single source to produce both spectra, as it is not possible to filter the high energy spectrum as describe previously for the dual source technique.

The GE HD750 (General Electric Medical Systems, Milwaukee, WI) is a commercially available DECT scanner that uses the rapid kVp switching technique. This system includes analysis software, the GSI [Gemstone Spectral Imaging] Volume Viewer (General Electric Healthcare, Milwaukee, WI), that allows for two material basis pair decomposition image sets to be reconstructed based on a user selected material basis pair. This system also includes MSI [Material Suppressed Iodine] analysis software that allows for the reconstruction of Virtual Unenhanced (VUE) images in which the iodine volume is replaced with an equivalent volume of blood to generate a virtual non-contrast data set from data acquired after the administration of iodine contrast. The focus of this study will be on assessing the functional capabilities of these VUE images generated from MSI software.

1.2 Classification of renal lesions

Abdominal multiphase CT exams are a commonly used non-invasive imaging technique for the classification of renal lesions [15]. The CT exams are often used to distinguish hyper-attenuating renal cysts from enhancing renal masses after a contrast agent is administered intravenously [3]. Multiphase renal CT exams include a non-contrast phase which is followed by the administration of a contrast agent, typically iodine based, and one or more post-contrast imaging phases. Iodine is commonly used as the contrast agent due to the high contrast it offers relative to the tissues in the human body. Enhancement can be quantified by comparing the measured CT number of a lesion in the non-contrast image to the measured CT number of the same lesion in the post-contrast image. Previously a difference of 10 HU between non-contrast and post-contrast images was the minimum criterion for enhancement [16]. However, with the advent of helical CT it has been suggested that this threshold of 10 HU should be increased to account for artifacts from helical interpolation, and enhancement is currently characterized definitively as a change in CT number of approximately 20 HU or greater between pre- and post-contrast phases [17]. The exact change considered to be positive for enhancement has not been universally agreed upon for helical CT, and may also vary depending on acquisition parameters, including position within the FOV and the calibration of the CT scanner used [18].

1.2.1 Renal Cell Carcinoma

Renal cell carcinoma (RCC) is the most common kidney cancer in adults, accounting for approximately 90% of renal neoplasms and 3% of all adult malignancies, and resulted in approximately 14,00 deaths in 2014 [19]. RCC is an aggressive disease that forms in the lining of the proximal tubular epithelium, and has a 5-year survival rate of 95% for stage 1 disease, but less than 20% for state 4 disease [20].

The diagnosis of RCC based on the appearance of the lesion on CT imaging can vary widely in difficulty. Diagnosis of a simple, non-enhancing cyst is straightforward while

classifying complex lesions is much more challenging [15]. In an effort to standardize the

classification and management of renal lesions, the Bosniak Classification system was proposed

in 1986 [16] and was updated in 2005 [16, 21]. A simplified description of the four classifications

for renal lesions according to the Bosniak system is given in Table 1 [21].

Category	Description
I	A benign simple cyst that uniformly measures water density and does not enhance
II	A benign cyst that may contain a few hairline thin septa in which "perceived" (not measureable) enhancement may be present. Cysts in this category do not require further evaluation.
IIF	A cyst that may contain multiple hairline thin septa and "perceived" enhancement may be present. Calcification may be present, but there is no measurable enhancement. Cysts in this category require further evaluation to prove benignity.
III	"Intermediate" cystic masses in which measurable enhancement is present. These are surgical lesions that may prove to be benign or malignant, such as RCC
IV	Clearly malignant cystic masses that meet criteria III and additionally contain enhancing soft-tissue adjacent to the wall or septum. These include cystic carcinomas and require surgical removal.

Table 1. Bosniak renal cyst classification system [21]

During a typical multiphase renal CT exam a patient undergoes an unenhanced scan,

followed by intravenous administration of a contrast agent and several post-contrast scans, some

of which may be delayed by several minutes to evaluate washout of the contrast. Studies have

shown that if the patient has an enhancing renal mass, such as RCC, the mass will have a

substantial non-calcified region with a CT number measuring within a range of 20-70 HU on

unenhanced CT, while normal renal parenchyma will measure approximately 30 HU [22]. In a

post-contrast scan acquired during the corticomedullary phase, studies have shown that RCC will

enhance significantly more than a benign cyst (112.9 HU vs 59.8 HU, respectively [23]) and that a difference of greater than 42 HU in the measured enhancement during the corticomedullary phase from the unenhanced phase was highly predictive of RCC [23]. During the corticomedullary phase, normal renal parenchyma will measure approximately 200-300 HU, which is greater than the typical post-contrast CT number of an RCC mass.

Imaging in the post-contrast phase may not allow for distinct differentiation of hyperattenuating cysts from renal neoplasms. Acquiring a delayed phase can demonstrate contrast washout, or de-enhancement, associated with a diagnosis of vascularity of the mass, allowing for differentiation of hyperattenuating cysts from renal neoplasms [24].

1.2.2 Angiomyolipoma

Accurate classification of renal masses is essential to prevent unnecessary medical intervention. As previously discussed, RCC is a dangerous disease and should be completely resected from the kidney when present. But there are some masses, commonly referred to as pseudotumors, which can mimic RCC on unenhanced CT scans. An example of a pseudotumor is angiomyolipoma (AML), which is the most common benign tumor of the kidney [25]. AML is commonly diagnosed by the detection of fat and the measurement of CT numbers on unenhanced CT scans. However, in approximately 4.5% of cases the mass is "lipid-poor" and no fat can be visualized on CT [26]. In these cases, AML is commonly suspected as being RCC and is treated unnecessarily. Thus, the ability of an unenhanced CT image to accurately reflect fatty characteristics of a mass is crucial.

1.3 Virtual Unenhanced Imaging

The material decomposition capability provided by DECT allows for the estimation of the amounts of two basis materials contained within each voxel of an image. An example of such a material basis pair is water and iodine. Virtual Unenhanced (VUE) imaging extends basis material decomposition to create a virtual pre-contrast CT dataset from a DECT acquisition.

Conceptually, basis pair material decomposition is performed into water and iodine projections, and then the calculated iodine concentration is removed and replaced with a suitable material [27]. In the VUE implementation, the material suppressed iodine (MSI) algorithm (General Electric Healthcare, Milwaukee, WI) estimates the volume of iodine contrast contained within each voxel and replaces it with an equivalent volume of blood, which is the material that iodine contrast has likely displaced in a post-contrast CT acquisition [27]. While this technique can be generalized to decompose an image into an arbitrary number of materials [10], the technique employed in VUE image reconstruction is believed to utilize a two-material decomposition technique [7].

This algorithm is based on a model that assumes the materials within each voxel mix to form an ideal solution, i.e., the volume of a mixture equals the sum of the volumes of the constituent materials [27]. Using this model, the linear attenuation coefficient for each voxel in the VUE image at a given energy can be described mathematically as [27]:

$$\mu(E) = \sum_{i=1}^{N} \alpha_i \mu_i(E)$$
Equation 1.3-1

where

$$\alpha_i = \frac{v_i}{\sum v_j} \quad \ni \quad \sum_{i=1}^{N} \alpha_i = 1$$
Equation 1.3-2

Since the materials in each voxel mix to form an ideal solution, the sum of the volume of contrast and the volume of blood in a mixture of contrast and blood would equal the volume of the total mixture. Based on the assumption that iodine displaces only blood, the volume of blood in the VUE image would be set equal to the volume of contrast in the post-contrast image. Therefore, the volume of contrast removed from each voxel is replaced with the equivalent volume of blood.

Since the development of the virtual unenhanced imaging reconstruction technique, many potential applications have been investigated. Such applications include:

- Replacement of pre-contrast images with virtual non-contrast images in

    o Renal DECT exams, the feasibility of which is the focus of this work

       [3, 7, 9, 28]

    o Liver DECT exams [29, 30]

    o DECT urography for detecting urinary stones [31, 32]

    o DECT cholangiography [33]

- Utilizing a virtual noncalcium technique in:

    o Detection of posttraumatic bone marrow lesions [34]

    o Detection of bone marrow edema in acute fractures [35]

- Radiotherapy treatment planning to improve dose calculations [36]

A prior study has compared a number of patient CT datasets using both true pre-contrast and virtual non-contrast datasets in multiphase renal exams with a dual-source DECT technique and has shown promising results [9]; however, a careful systematic evaluation of this technique has not been completed which is the focus of this work. This study also evaluats a different DECT acquisition technique and reconstruction algorithm for generating virtual non-contrast datasets. Some prior studies are based on a three-material decomposition algorithm used for VUE image reconstruction, whereas this study will focus on a two-material decomposition algorithm [7, 9].

1.4 Motivation

There are several potential benefits to be realized from replacing true unenhanced (TUE) images with virtual unenhanced (VUE) images during multiphase renal CT exams. The first, and perhaps most significant, is the reduction in patient radiation dose. Previous studies have demonstrated that reductions in radiation dose can be as great as 35% [9]. Second, eliminating the pre-contrast phase would reduce the exam time for each patient and consequently could increase patient throughput and clinical efficiency. Finally because VUE images are reconstructed from post-contrast images, a pre-contrast scan would no longer need to be registered to the post-

contrast scans, which would potentially reduce misregistration and differences in partial volume averaging between the pre- and post-contrast scans [37].

These potential benefits motivated this study, which assessed the feasibility of replacing TUE images with VUE images reconstructed from post-contrast images acquired using DECT. As previously discussed, characterization of renal masses is a complicated and sometimes equivocal process, and therefore the quality of VUE images must be carefully assessed to ensure that diagnostic quality is maintained.

Chapter 2. Hypothesis

2.1 Statement of Hypothesis

Classification and quantitative evaluation of renal lesions is not significantly different when using virtual unenhanced images (VUE) in place of true unenhanced images (TUE) based on a p-value of 0.05. Additionally, classification of images based on enhancement measurements will not be different when using VUE images versus TUE images for the baseline measurement across a wide range of clinical scenarios based on a posterior probability of 0.05 for negative significance and 0.95 for positive significance using a mixed effects model.

2.2 Research Approach

In order to test this hypothesis, the project was divided into three specific aims. Each aim contributed to testing the stated hypothesis.

Specific Aim 1: A retrospective study of 60 patient exams was conducted for qualitative and quantitative evaluation of VUE and TUE images.

- Sub aim 1.1: Three radiologists were presented with VUE and TUE images for qualitative evaluation. The results were analyzed with a Bayesian Hierarchical model to determine if VUE images were significantly different from TUE images.

- Sub aim 1.2: VUE images were compared to TUE images by using quantitative measurements of specific regions of interest in each of the 60 unique patient exams. These regions of interest included liver, aorta, spleen, spine, cystic lesions (if present), subcutaneous fat, and the renal cortex and medulla. The results were compared using a paired t-test.

Specific Aim 2: Characterization of lesions using VUE images compared to TUE images was assessed using a set of three patient-mimicking phantoms. These phantoms were used to acquire an extensive data-set for the comparison of lesion characterization in each under varying conditions.

14

- Sub aim 2.1: Three phantoms were constructed specifically for this research project to represent patients of small, medium, and large sizes.

- Sub aim 2.2: The medium phantom was used to acquire images with a fixed configuration (i.e., one lesion size in a specific position in the SFOV) and variation only in the GSI protocol used. The acquired images were evaluated to determine up to five candidate GSI protocols that were to be used for evaluation of the medium and small phantoms. This same process was repeated to determine candidate GSI protocols for evaluation of the large phantom.

- Sub aim 2.3: All phantoms were imaged in different configurations using the GSI protocols identified in Sub aim 2.2. The variables in configuration setup included location of the lesion within the SFOV, lesion size, phantom size, image thickness, contrast concentration, and selected GSI protocol. The results were analyzed using a Bayesian Hierarchical model.

- Sub aim 2.4: A set of up to 3 optimal clinical GSI protocols will be identified and recommended for clinical use in clinical multiphase DECT for renal evaluation, if differing from current clinically used protocols.

Specific Aim 3: The effect of ASIR (adaptive statistical iterative reconstruction) on VUE CT number measurements was evaluated.

- Sub Aim 3.1: A subset of images acquired in Sum Aim 2.3 were used to reconstruct VUE images with varying levels of ASIR under varying conditions. The variables in configuration setup included location of the lesion within the SFOV, lesion size, phantom size, image thickness, contrast concentration, and selected GSI protocol. The variation in reconstruction technique involved application of 0%, 60%, and 100% ASIR levels for each phantom configuration. The results were analyzed using a mixed effects model.

Chapter 3. Methodology

3.1 Specific Aim 1 Methods

Virtual unenhanced images were reconstructed from DECT data sets for 60 consecutive patient exams using version 2.0 of the GE AW Server. A single source multi-detector row GE Discovery CT750HD (General Electric Healthcare, Milwaukee, WI) scanner was used to acquire the patient exams, an example of which is shown in Figure 2. This system consisted of one X-ray tube which rapidly switched between two energy spectra and a corresponding 64-channel detector with 0.625 mm channel width. The DECT data set was then loaded onto the dedicated DECT post-processing workstation (AW Server, version 2.0; General Electric Healthcare) for reconstruction. The multi-material decomposition algorithm, referred to as Material Suppressed Iodine (MSI), was then applied to post-contrast images in the GSI Volume Viewer (General Electric Healthcare, Milwaukee, WI), to reconstruct the VUE images. Each image was reconstructed at 3.75 mm thickness, 2.5 mm interval, and a DFOV identical to that used to acquire the TUE. VUE images were reconstructed for all 60 patient cases, for a total of 120 images (60 VUE and 60 TUE) for analysis.
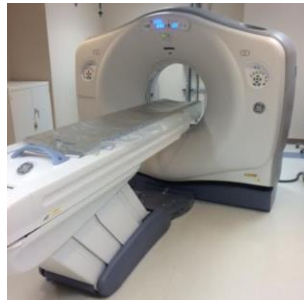
Figure 2. GE Discovery CT750HD Scanner

60 standard of care patient examinations with an indication of pancreatic lesions were consecutively selected for retrospective analysis. The demographics of the patients examined are given in Table 2.

	N	Mean age (yrs)	Age range (yrs)	Mean BMI (kg/m^2)
Male	33	63	39 - 77	25.7
Female	27	60	33 - 79	27.1
Total	60	62	33 - 79	26.3

Table 2. Demographic Information for Patients used in Retrospective Study

An unenhanced scan of each patient was first acquired using 120 kVp with tube current modulation, a pitch of 0.984, and a gantry rotation time of 0.8 s. The iodine contrast agent was administered intravenously at an injection rate of 4cc/sec (125 cc total) with a delay of 40 seconds and a DECT dataset was acquired during the arterial phase. A pitch of either 0.516 or 0.984 was used with a corresponding gantry rotation time of 0.5 s or 0.8 s, respectively. The DECT dataset was acquired using beam energies of 80 kVp and 140 kVp. The interleaved high and low projections were used to generate water and iodine attenuation maps, which were then used for VUE image reconstruction.

The patient cases used for Specific Aim 1 were standard of care, and were analyzed retrospectively. As a consequence the raw data were not available for image reconstruction; therefore it was not possible to exactly match reconstruction parameters between TUE and VUE images. This was problematic in particular because different reconstruction kernels and different levels of iterative reconstruction (Adaptive Statistical Iterative Reconstruction [ASIR], General Electric Healthcare) were applied to the TUE images and the DECT dataset. TUE images were reconstructed with the SOFT kernel and 60% ASIR, whereas the VUE images were reconstructed with the STANDARD kernel and 0% ASIR. This variation in reconstruction is a limitation of the study, as it may have affected the qualitative comparison of VUE to TUE images.

3.1.1 Sub aim 1.1

A qualitative comparison of VUE and TUE images was conducted with three experienced radiologists. Images were blinded as to method of reconstruction and presented to each radiologist individually. Each radiologist was asked to complete a questionnaire for each image presented. The full survey presented with the associated instructions are provided in Appendix 6.1. The survey evaluated the following image characteristics using a Likert scale:

1. Visualization of major vessels (considering hepatic, portal, and renal veins in particular)
2. Visually sharp reproduction of the pancreatic contour
3. Visualization of calcifications
4. Depiction of liver parenchyma, e.g., ability to determination of the degree of fatty infiltration
5. Visualization of adrenal glands
6. Corticomedullary differentiation

A random subset of 15 patient cases was selected to be repeated to quantify intra-observer variability. The complete set of images presented to each radiologist included 150 images in total (60 VUE and 60 TUE unique images, as well as 15 repeated VUE images and the corresponding 15 repeated TUE images). Each radiologist completed the retrospective evaluation in multiple sessions to minimize fatigue. The data from this study were analyzed using a Bayesian Hierarchical model.

3.1.2 Sub aim 1.2

A quantitative comparison of the TUE and VUE images was conducted using the version 2.0 of the GE AW Server. Each TUE image was non-rigidly registered to the corresponding VUE image prior to ROI placement using the "Integrated Registration" feature of the post-processing workstation. ROI measurements were made in the following anatomical regions in all images:

- Liver

- Abdominal aorta

- Inferior vena cava

- Spleen

- Spine

- Renal medulla

- Renal cortex

- Cystic lesion (if present)

- Subcutaneous fat

Notice that the selected regions were anatomically different, comprising tissues of differing density and attenuation properties for analysis of the impact of the MSI algorithm on tissues with varying amounts of iodine contrast on board. Theoretically the spine and subcutaneous fat should be minimally affected by the MSI algorithm because these regions generally do not uptake iodine contrast.

Regions of interest placed in each tissue ranged in area from 30 mm^2 to 700 mm^2, depending on the size of the anatomical structure. Examples of ROI placement are shown in Figure 3. The data from this study were analyzed using a student's paired t-test.
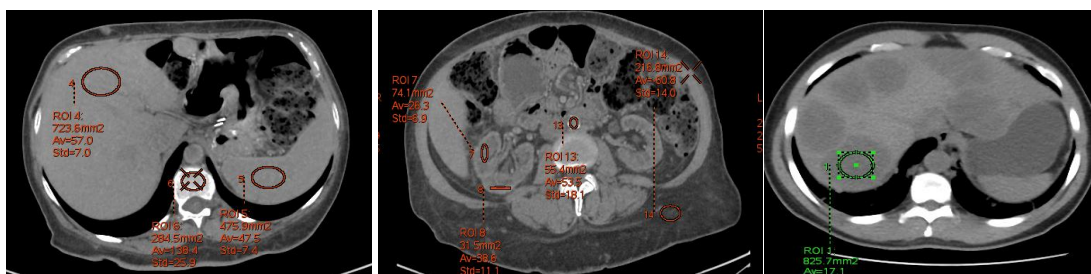
Figure 3. Example ROI placement for quantitative measurements, from left to right: (left image) liver, spine, spleen; (center image) renal cortex, renal medulla, abdominal aorta, subcutaneous fat; (right image) cystic lesion

3.2 Specific Aim 2 Methods

A phantom study was conducted to assess the accuracy of lesion characterization when using VUE images in place of TUE images. Phantoms were constructed at the MD Anderson Center for Advanced Biomedical Imaging (CABI) machine shop. The phantoms were used to acquire an extensive data-set for lesion characterization across varying conditions. The GE Discovery CT750HD DECT scanner with Gemstone Spectral Imaging (GSI) capability located at CABI was used for all data acquisition and the GE AW workstation was used for all image processing.

3.2.1 Sub aim 2.1

Three phantoms were constructed to represent patients of small, medium, and large sizes. Each phantom contained the following:

- Delrin rod 3.67 cm in diameter to mimic patient spine

- Insert for PMMA hollow sphere 1.0 cm in diameter located to the right of the spine

- Insert for 3 PMMA hollow spheres of diameter 1.0, 2.0, and 3.0 cm located in the periphery of the phantom. The three different size inserts allowed for assessment of variation of lesion size on enhancement accuracy. Additionally, the 1.0 cm sphere was compared to the 1.0 cm sphere located in the right kidney region for evaluation of the effect of lesion position within the field of view (FOV) enhancement accuracy.

- Insert for PMMA cylinder 1.0 cm in diameter located to the left of the spine

The distance of each insert from the Delrin rod (spine) varied depending on patient size. All phantoms were composed of four elliptical plates that were 5 cm thick, yielding a total length of 20 cm for all phantoms. An axial section of the design for each phantom, including the distance of each insert from the Delrin rod, is given in Appendix 6.2.
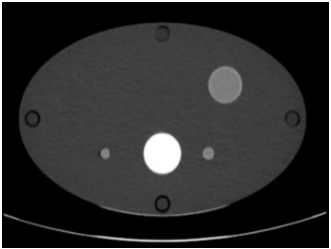
Phantom Size	Phantom Dimensions (cm)		
	Major Axis	Minor Axis	
Small	28.3	17.4	
Medium	36.1	22.2	
Large	47.9	29.4	

Table 3. Phantom Dimensions

The dimensions of each phantom are displayed in Table 3 and were based on the 5th (small), 50th (medium), and 95th (large) percentiles of the United States population from the People-Size 2008 visual anthropometry software (Open Ergonomics Ltd, Leicestershire, UK). An example CT image of the medium phantom with the 3 cm outer sphere, 1 cm inner sphere, and 1 cm rod insert in place is included in Table 3. Each phantom was composed of four 5 cm thick high density polyethylene (HDPE) elliptical plates. Three sets of the two central plates for each phantom were constructed to accommodate the 1, 2, and 3 cm outer spherical inserts, which simulated variation in lesion size, pictured in Figure 4.
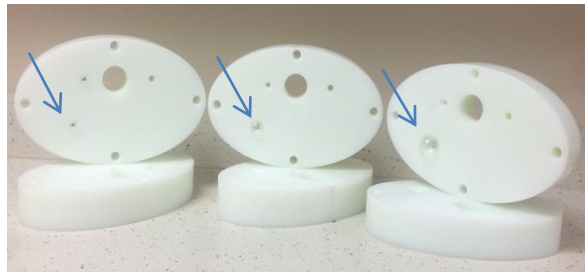
Figure 4. The three sets of exchangeable phantom plates for the small phantom, which accommodated spherical lesions of varying diameter. Each set served as the center two plates of the phantom, and could be exchanged to allow for different lesion sizes

Figure 5. Custom designed small phantom fully assembled (left image), the center two plates (center image), and half assembled (right image)

3.2.2 Technical Notes

3.2.2.1 Relationship between CT number and iodine concentration

For phantom experimentation, a relationship between CT number and iodine concentration was determined. Variation in energy spectra across CT scanners makes analytic calculation of this relationship difficult; therefore it was determined experimentally. Previous experiments had shown that for a 120 kVp beam the relationship between iodine concentration and CT number can be expressed as [38]:

$$Iodine\ concentration\ \left(^{mg}/_{mL}\right) = 0.0365 * (CT\ number) - 0.85 \qquad \text{Equation 3.2.2.1-1}$$

Using this relationship as a baseline for developing the methodology for this experiment, six Optiray 320 (Mallinckrodt Pharmaceuticals, St. Louis, MO) and water mixtures were chosen, as given in Table 4. The medium phantom with the 3 cm diameter insert, which had a volume of 14.1 mL, was used for each trial. The iodine concentration for each mixture was calculated using the volume of the insert, as well as the concentration of Optiray 320, which contained 320 mg/mL organically bound iodine. The volume of Optiray 320 was measured using a 2 mL volumetric pipette, which had a reported uncertainty of ± 0.01 mL. Images were acquired with the GE HD750 DECT scanner using the GSI-37 DECT protocol (medium body filter, 0.8 sec rotation time, 40 mm beam width, 0.984 pitch, 260 mA, and a CTDI$_{vol}$ of 10.99 mGy) and a 2.5 mm

image thickness. For each trial, the mean CT number (HU) and standard deviation were recorded from a circular region of interest (ROI) of approximately 150 mm^2 drawn in the center of the 3 cm sphere in the central axial image through the sphere. The ROI was propagated through the two images superior and inferior to the central image for a total of five ROI measurements on consecutive slices. The average of these measurements was computed and linear regression was used to calculate the relationship between CT number (HU) and iodine concentration (mg/mL) for the CT scanner used in this study.

Trial	Optiray (mL)	Concentration of Optiray by volume (%)	Concentration of Water by volume (%)	Iodine Concentration (mg/mL)
1	0.14	0.99	99.01	3.17
2	0.28	1.98	98.02	6.34
3	0.42	2.97	97.03	9.51
4	0.56	3.96	96.04	12.68
5	0.70	4.95	95.05	15.84
6	0.84	5.94	94.06	19.01

Table 4. Iodine concentrations used for experimentation

3.2.2.2 Phantom set-up verification

As discussed in section 1.2.1, renal cell carcinoma (RCC) has been shown to enhance from the range of 20-70 HU in the pre-contrast image to approximately 110 HU in the corticomedullary phase [22, 23], while normal kidney parenchyma enhances from approximately 30 HU to 200-300 HU. As a result, in an actual patient exam TUE images will be obtained when the renal mass has an attenuation approximately equal to or greater than the surrounding renal tissue, and VUE images are reconstructed from DECT data acquired when the renal mass has

attenuation less than that of the surrounding normal tissue. In practice, the DECT image is acquired with the renal mass in a positive enhancing background, whereas with the phantom constructed for this study simulated renal masses in a negative contrast background. The potential impact of the differences between clinical CT and the phantom study was evaluated using the Jaszczak Phantom (Biodex, Shirley New York) imaged in two configurations, one mimicking the expected patient scenario and the other mimicking the phantom scenario, the details of which are given in Table 5. The Jaszczak phantom was configured with three hollow spheres of different sizes (Table 5 and Figure 6). The relationship between CT number and iodine concentration determined experimentally (section 4.2.1.1) was used to calculate the amount of iodine contrast necessary to achieve the desired CT number.

	Sphere	Background	
Experiment 1: Patient set-up	Iodine-water mixture (100 HU)	Iodine-water mixture (250 HU)	
Experiment 2: Phantom set-up	Iodine-water mixture (100 HU)	Water (0 HU)	

Table 5. Jaszczak Phantom Experiment
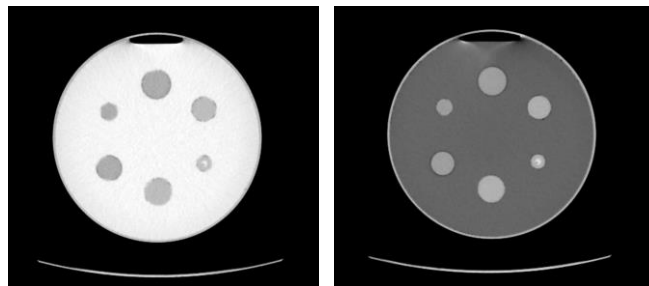
Figure 6. Example images from the Jaszczak phantom experiment. An expected patient scenario for post-contrast imaging in the corticomedullary phase was simulated (left), as well as the phantom set-up (right)

DECT Images were acquired with the GE HD750 scanner using the GSI-11 DECT protocol (medium body filter, 36 cm DFOV, 0.8 sec rotation time, 40 mm beam width, 600 mA,

0.984 pitch, and a CTDI$_{vol}$ of 26.70 mGy) and a 2.5 mm image thickness. VUE images were

reconstructed from all DECT images. For each experiment, the mean CT number (HU) and

standard deviation were recorded from a circular region of interest (ROI) of approximately 150

mm^2 for the 31.8 mm diameter sphere and 100 mm^2 for the 25.4 mm diameter sphere drawn in the

central axial image through the sphere. The ROI was propagated through the two images

immediately superior and inferior to the central image to yield ROI measurements on five

consecutive images.

3.2.3 Sub aim 2.2

A single configuration was selected for imaging the medium phantom, so as to bridge the

retrospective study to the phantom study. The parameters selected were informed by techniques

used to acquire the unenhanced and DECT images in the retrospective study, and are listed in

Table 6. All available GSI protocols on the GE CT750HD scanner for the medium size bowtie

were used for image acquisition. A complete list of the presets used is given in Appendix 6.3.

Parameter	Medium Phantom (DECT)	Medium Phantom (TUE)
Image thickness	5.0 mm	5.0 mm
DFOV	400	400
Pitch	0.984	0.984
kVp, mAs	GSI protocol dependent	120, 150
Lesion diameter	3 cm	3 cm

Table 6. Imaging parameters for the single phantom configuration used for comparison of

GSI protocols

The phantom inserts were filled with an Optiray 320 and water mixture with 3.38 mg/mL iodine concentration to simulate approximately 80 HU enhancement for DECT image acquisition, and with water only for TUE image acquisition. The following equation was used to convert the calculated iodine concentration necessary to simulate a given CT number to Optiray 320 concentration:

$$\boldsymbol{Optiray\ (mL)} = \frac{\boldsymbol{iodine\ (mg/mL) * total\ volume\ (mL)}}{\boldsymbol{320\ (mg/mL)}}$$
<div align="right">Equation 3.2.3-1</div>

VUE images were reconstructed from DECT images and compared to TUE images acquired with water only in the inserts. The intention of this experiment was to determine which GSI protocol produced VUE images in which measured CT numbers most closely matched those in TUE images, and then to use this information to identify 3-5 candidate protocols for further evaluation. CT numbers and their associated standard deviations were measured from a circular ROI placed in the center of each insert as well as in the spine of the phantom for VUE and TUE images. The dimensions of the ROIs placed for each image are given in Table 7.

ROI Location		ROI size (mm^2)
Center insert		14.4
Peripheral insert	1 cm	14.4
	2 cm	70-80
	3 cm	140-150
Hollow rod insert		6.0
Delrin rod		320-350

Table 7. Dimensions of ROI placement for each measurement location in TUE and VUE images

3.2.4 Sub aim 2.3

Phantoms were imaged in different configurations using the GSI protocols identified in
Sub Aim 2.2, which are listed in section 4.2.2. The following parameters were varied to assess the
effect of patient specific factors on the accuracy of enhancement measurements assessed using
DECT:

- *Patient size*: As discussed previously, variation in patient size was evaluated by imaging
  three phantoms of different sizes. The dimensions of each phantom are listed in Table 3.
- *Lesion size*: Hollow spheres of 1 cm, 2 cm, and 3 cm diameter were used to simulate
  variation in lesion size.
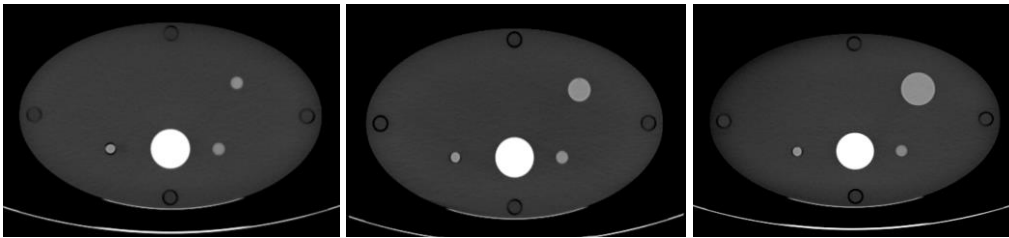
Figure 7. Variation in lesion size for the small phantom

- *Position within the field of view (FOV)*: Each phantom also contained a 1 cm hollow
  sphere near the spine insert in addition to the 1 cm sphere mentioned in the previous
  section, which was located in the periphery of the phantom. These spheres were used to
  study the effect of position within the FOV on enhancement accuracy. The distance of
  each lesion from the Delrin rod increased proportionally with increasing phantom size.
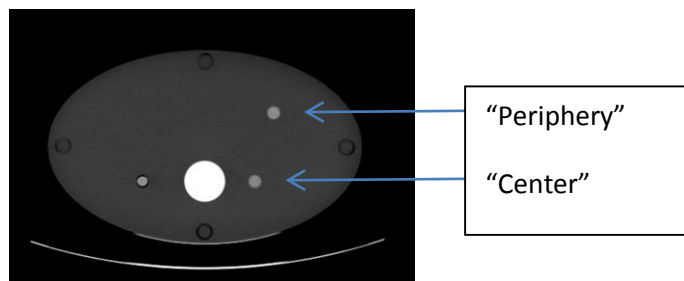
Figure 8. Variation of position of the lesion within the FOV

- *GSI protocol*: As determined in Sub Aim 2.2, GSI protocols 10, 11, 16, and 29 were used for the small and medium phantoms and GSI protocols 10, 12, 22, 36 were used for the large phantom to study the impact of GSI protocol on quantitative accuracy of DECT. The parameters associated with each of these protocols are listed in Table 19.

- *Enhancement magnitude*: The purpose of varying contrast concentration was to assess VUE enhancement accuracy across a wide range of simulated clinical scenarios. The clinical scenarios used to vary iodine concentration are detailed in the following sections.

The most common method for classifying renal lesions is the Bosniak criteria [19]. These guidelines provide a method for categorizing cystic lesions based on several characteristics including enhancement of the lesion, which has been stated to be the most important criterion used in determining surgical from non-surgical renal masses [17]. Consequently, it is crucial that CT numbers measured in pre- and post-contrast images are accurate. This motivated the incorporation of variation in iodine concentration as a parameter of interest in the phantom study. Five clinical scenarios were simulated, each of which are detailed in the following sections.

For each simulation, the concentration of Optiray 320 necessary was determined using the relationship between CT number and iodine concentration given in 4.2.1.1. Optiray 320 was measured for each solution using a 2 mL volumetric pipette with an associated uncertainty of ± 0.01 mL. Images were then acquired using the GE HD750 DECT scanner. VUE images were reconstructed from DECT data and then CT number, as well as the associated standard deviation of the measurement, was recorded from ROI placement in various regions of the phantom. The dimensions of the ROIs for each measurement location are listed in Table 7. The data were analyzed using a mixed effects model that accounted for both fixed and random effects, which is further discussed in 4.2.4. In Clinical Scenarios 1 and 2, VUE images were reconstructed from DECT images and were compared to TUE images acquired using SECT. A conceptual explanation of the experimental design for Clinical Scenarios 3-5 is given in Table 8. Further explanation regarding the solutions used to simulate each scenario is detailed in the following

sections. An example of the image acquisition matrices for SECT images and for DECT is provided in Appendix 6.4.

	Pre-contrast		Post-contrast	Analysis
TUE (SECT)	Acquired as "baseline" with no Optiray 320	SECT	Acquired with the specified concentration of Optiray 320	Enhancement = SECT – TUE
VUE (DECT)	Reconstruction from DECT post-contrast images	DECT	Acquired with the specified concentration of Optiray 320	Enhancement = DECT – VUE

Table 8. Conceptual description of the experiment design for Scenarios 3-5

Scenario 1

A fatty lesion was simulated to mimic angiomyolipoma (AML), which is a non-surgical renal pseudotumor that can mimic a mass requiring surgery, such as renal cell carcinoma. This simulation allowed for assessment of the ability of VUE images to accurately represent fatty lesions. As discussed in section 1.2.2, this simulation represented a clinical scenario in which it is crucial to distinguish AML from RCC to avoid unnecessary intervention.

The AML lesions were simulated by filling the inserts for the phantom with vegetable oil, yielding a CT number of approximately -100 HU. All images were acquired with only vegetable oil in the spheres.
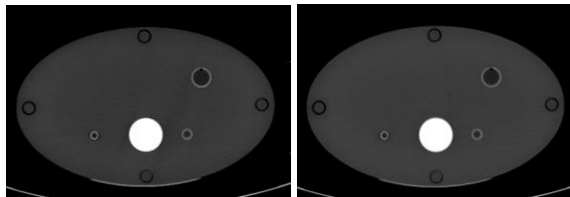
Figure 9. TUE (left) and VUE (right) of small phantom for Scenario 1

This scenario, along with those to follow, served to simulate the categories of the Bosniak criteria, which are detailed in Table 1. Category I of the Bosniak criteria describes a benign simple cyst that measures water density and does not enhance [21]. Simple benign cysts were simulated by filling the phantom inserts with distilled water. All images were acquired with only distilled water in the spheres.
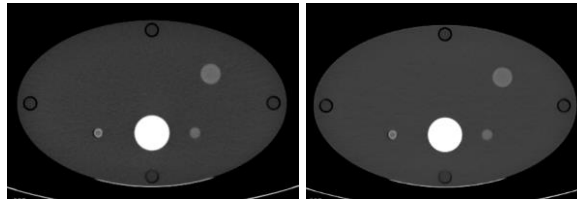
Figure 10. TUE (left) and VUE (right) of small phantom for Scenario 2

Scenario 3

Category II-IIF of the Bosniak criteria describes a benign cyst in which enhancement may be perceived, and those in category IIF require follow-up studies to prove benignity [21]. In order to simulate a lesion that is likely benign, but requires further investigation to prove benignity, such as a category IIF cyst, a baseline attenuation of 20 HU was simulated to represent the pre-contrast phase of imaging. A 20 HU baseline was chosen because it represented a borderline measurement for identification of RCC on a TUE image, which typically measures in the 20-70 HU "danger zone" in the pre-contrast imaging phase [22]. For post-contrast simulation, Optiray 320 was added to the solution to simulate a small amount of enhancement. For a lesion in this category, enhancement may be perceived but would be minimal [21]. As discussed in section 1.2, it was previously believed that 10 HU was the threshold for enhancement determination, but with the advent of helical CT it was proposed that this threshold be increased to 15 or even 20 HU, and there is currently no universal agreement on this matter [16, 17]. Considering this, two enhancement scenarios were simulated for this experiment to represent a low "perceived"

enhancement of 5-10 HU and a borderline, or intermediate, enhancement of approximately15-20 HU.

The baseline images for this scenario were acquired with an apple juice and water mixture to simulate an attenuation of 20 HU. Apple juice was chosen for simulation in this and the subsequent scenarios as a surrogate for blood because it has an effective atomic number, density, and CT number that is very similar to blood. Optiray 320 was then added to the mixture to simulate each enhancement scenario, and the SECT and DECT post-contrast images were acquired. The Optiray 320 concentrations necessary to simulate these levels of enhancement were calculated based on the relationship determined in section 4.2.1.
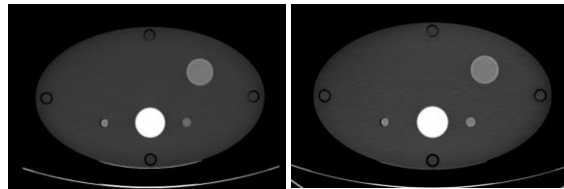
Figure 11. TUE (left) and VUE (right) of small phantoms for Scenario 3, VUE image pictured was reconstructed from the intermediate enhancement DECT image

Scenario 4

A Bosniak Category III lesion is intermediate that requires further work-up, for example a lesion measuring approximately 40 HU on a pre-contrast image and exhibiting slight enhancement in post contrast images. An attenuation of 40 HU was chosen for this scenario as well as for Scenario 5 because a recent study has shown that the attenuation of renal neoplasms as measured by a radiologist was on average 38.4 HU [39]. Two enhancement scenarios were simulated to represent low enhancement (5-10 HU) and intermediate enhancement (15-20 HU). As previously stated, the aim of scenarios 3-4 was to simulate borderline lesions for comparison of TUE to VUE as the baseline image for enhancement measurements, which is where the accuracy of an enhancement calculation is the most crucial.

The baseline SECT images were acquired with an apple juice/water mixture (with a CT number of approximately 40 HU) in the inserts and the DECT images were acquired with Optiray 320 added to the mixture, as described previously.
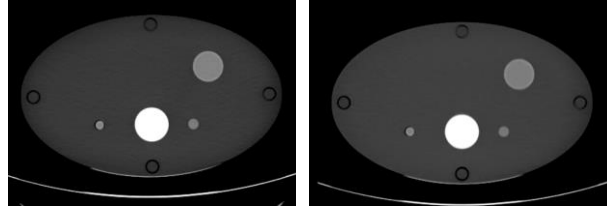
Figure 12. TUE (left) and VUE (right) of small phantom for Scenario 4, VUE image pictured was reconstructed from the low enhancement DECT image

Scenario 5

Bosniak Category IV describes a lesion that is clearly malignant and enhances substantially [21]. A lesion in this category will exhibit high vascularity and consequently demonstrate substantial uptake of iodine contrast in post-contrast imaging, resulting in significant enhancement. An enhancement of approximately 40-50 HU was chosen for simulation because it demonstrates definitive enhancement and is in the range of typical enhancement of RCC. A previous study has shown that clear cell renal carcinoma (cRCC) and papillary renal cell carcinoma (pRCC) enhance to a mean of 149 and 91 HU, respectively, in the corticomedullary phase and 95 and 71 HU, respectively, in the nephrographic phase [40].

This was simulated by using apple juice/water mixture for the baseline unenhanced image. Optiray 320 contrast was then added to the mixture to result in a total attenuation of 80 HU, which corresponded to an enhancement of 40 HU.
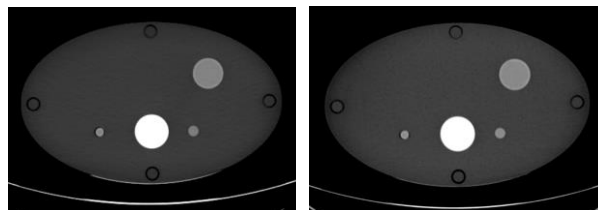
Figure 13. TUE (left) and VUE (right) of small phantoms for Scenario 5

For each scenario, CT number and image noise were measured in all inserts. The data collected were analyzed using a mixed effects model, chosen to account for fixed and random effects in the study. The details of this model are given in section 4.2.4. A summary of the five clinical scenarios simulated is given in Table 9.

Clinical Scenario	TUE baseline (HU)	Enhancement (HU)	Purpose:
Fatty lesion	-100	None	Ability to distinguish fatty lesions
Bosniak I	0	None	Ability to distinguish a benign simple cyst
Bosniak II-IIF	20	5-10, 15-20	Assess lesion enhancement accuracy
Bosniak III	40	5-10, 15-20	
Bosniak IV	40	40-50	

Table 9. Summary of clinical scenarios for experiments

An evaluation of the sources of variation in the measurements was necessary to account for random effects in the mixed effects model. The potential sources of random error were identified as preparation of the solutions and phantom set-up (σ_P), scanner variability (σ_S), variation between images in each acquisition (σ_M), and variation across the ROI, or quantum noise (σ_N).

Variation in preparation of the solutions (σ_P) was controlled for in the design of the experiments. For each prepared solution all images needed for all phantom configurations for that particular solution were acquired using a single preparation of inserts. That is, one mixture was created and used for all imaging; therefore limiting uncertainty due to systematic error, which was associated with the use of a volumetric pipette to measure the Optiray 320 concentrations, which had a reported uncertainty of $\pm$ 0.01 mL.

The random error of the CABI CT scanner (σ_S) was evaluated by using the QC data collected daily on the scanner over the course of two months. This analysis only considered the CABI CT 750HD scanner because it was the only scanner used for image acquisition in these experiments. The mean of the CT number measurements recorded for water each day was calculated, as well as the associated standard deviation. The standard deviation was then used to calculate the standard error (σ_S).

Variation between ROI measurement locations within the simulated lesion (σ_M) was considered as a source of random error. This was quantified by randomly selecting images from the experiment, and repeating CT number measurements 10 times in each region of interest. The standard deviation of the mean was computed, and then used to calculate the standard error. The standard error was < 0.1 in all cases, and was therefore considered to be negligible. This conclusion is expected considering the size of the ROI placed relative to the diameter of the spherical inserts constrained variation. Note that image-to-image variation was not considered because of the size of the spherical inserts relative to the 5.0 mm thickness of the images. Given that measurements were made in the 1 cm sphere for all images, there was only one image in each case where measurements could be made with minimal partial volume effect.

The SE associated with quantum noise (σ_N) was quantified by calculating the standard error of the mean CT number. For Scenarios 1 and 2, this was done using the recorded the standard deviation of each ROI measurement and the calculated number of pixels in each ROI. This could not be done for Scenarios 3, 4, and 5 because the result used for analysis was the difference between pre- and post- contrast measurements, i.e. the enhancement value. Notice that a standard deviation was recorded for each pre- and post-contrast measurement. In order to determine σ_N for these scenarios, the standard error was calculated for each pre- and post-contrast measurement and the results were added in quadrature [41]:

34

$$\sigma_N = \sqrt{\left(\sigma_{pre}\right)^2 + \left(\sigma_{post}\right)^2}$$

Equation 3.2.4-1

The total variation was then calculated by adding each source of variation in quadrature for each measurement. The estimated variation used as the input for random error in the mixed effects model is shown in equation 3.2.4-2.

$$\sigma_{total} = \sqrt{(\sigma_S)^2 + (\sigma_N)^2}$$

Equation 3.2.4-2

3.2.5 Sub aim 2.4

The purpose of this sub aim was to determine a set of up to three optimal GSI protocols to recommend for clinical DECT image acquisition, which could be used to reconstruct VUE images. This was not done because the results of this study do not support the clinical replacement of TUE images with VUE images.

3.4 Specific Aim 3 Methods

An evaluation of the effect of ASIR (adaptive statistical iterative reconstruction) on CT number accuracy of the VUE images was conducted. ASIR is a form of iterative reconstruction that begins after a first pass of filtered back projection reconstruction is completed, which shortens the time of reconstruction as compared to purely iterative techniques. The potential benefit driving clinicians to use ASIR is the reduction in noise, which could allow for reduction in the mA required to maintain diagnostic image quality, and consequently a reduction in patient dose.

A subset of the images acquired in Sub Aim 2.3 was used for this experiment to assess the impact of ASIR levels under varying phantom configurations. The variables selected to be assessed for this experiment were informed by observations made from Sub Aim 2.3 data. For each phantom configuration used, images were reconstructed with 0%, 60%, and 100% ASIR levels. The variables considered for this experiment were:

- Patient size: small, medium, and large

- Lesion size: 1 cm and 3 cm

- GSI protocol: the same protocols used in Sub Aim 2.3 will be assessed in this experiment

- Contrast concentration: 20 HU baseline lesion with 15-20 HU enhancement and 40 HU baseline lesion with 40 HU enhancement

- ASIR level: 0%, 60%, 100%

For each image set acquired CT number and noise were measured on the GE AW workstation in the spherical inserts as well as the Delrin rod, which mimics spine. The dimensions of the ROIs drawn for measurements are given in Table 7. Results were analyzed using a mixed effects model, the details of which are given in section 4.2.4.

Chapter 4. Results

4.1 Specific Aim 1

A retrospective analysis of 60 patient cases, with quantitative and qualitative comparisons, was conducted to statistically test the feasibility of replacing TUE with VUE images.

4.1.1 Results: Sub Aim 1.1

The qualitative study was based on a questionnaire given independently to three experienced radiologists for a total of 150 images (75 TUE and the corresponding 75 VUE images). Figure 14 presents a comparison of the mean scores between TUE and VUE images for all radiologists and patient exams for each question. Recall that questions 1-5 were based on a 5 point scale, and question 6 was based on a 3 point scale.
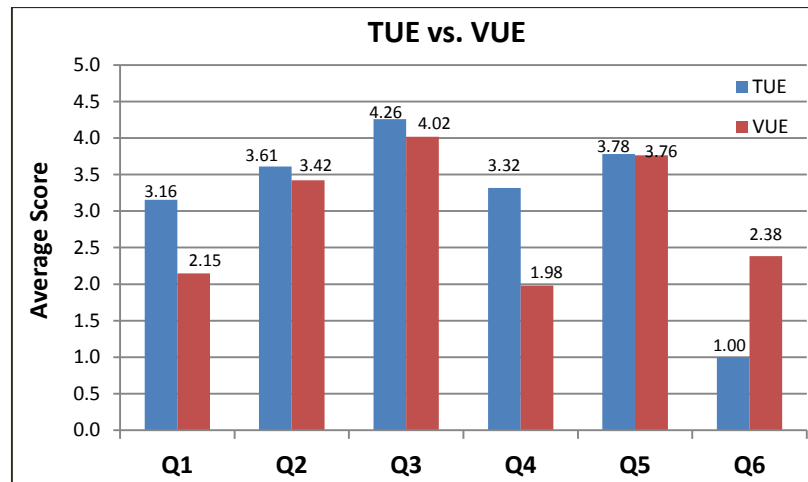
Figure 14. Comparison of mean TUE and VUE scores

The results were fitted with a Bayesian Hierarchical model to determine if VUE images were non-inferior to TUE images. This model was used for analysis to quantify and account for uncertainties, such as inter- and intra-observer variability. The results from this analysis are given in Table 10.

Question	Mean Difference (β)	Standard Deviation	95% Credible Interval
Q1 [Visualization of Vessels]	-0.514	0.055	(-0.624, -0.408)
Q2 [Pancreatic Contour]	-0.092	0.051	(-0.195, 0.004)
Q3 [Visualization of Calcifications]	-0.127	0.047	(0.216, 0.029)
Q4 [Depiction of Liver Parenchyma]	-0.682	0.052	(-0.786, -0.582)
Q5 [Visualization of Adrenal Glands]	-0.013	0.048	(-0.104, 0.084)
Q6 [Corticomedullary Differentiation]	1.379	0.039	(1.304, 1.455)

Table 10. Qualitative study results from the Mixed Effects Model Analysis

Intra-observer variability was calculated for each radiologist individually. This parameter was evaluated based on the random subset of 15 patient exams that were repeated during the study. The associated variability is included in the mixed effects model analysis, as described above. The results for each radiologist are shown in the figures in Appendix 6.5.

In addition to the mixed effects model analysis, the Kappa statistics for intra-observer variability were calculated for each radiologist and the results are shown in Tables 11-12.

.	Radiologist 1		Radiologist 2		Radiologist 3	
	Kappa Coefficient	Strength of Agreement [42]	Kappa Coefficient	Strength of Agreement [42]	Kappa Coefficient	Strength of Agreement [42]
Q1 TUE	0.386	Fair	0.079	Slight	0.566	Moderate
Q2 TUE	0.327	Fair	0.355	Fair	0.634	Substantial
Q3 TUE	0.339	Fair	0.259	Fair	-0.059	Less than chance
Q4 TUE	0.502	Moderate	0.336	Fair	0.639	Substantial
Q5 TUE	0.472	Moderate	0.101	Slight	0.348	Fair
Q6 TUE	1.00	Perfect	1.00	Perfect	1.00	Perfect

Table 11. Kappa Statistics for Intra-observer Variability (TUE images)

Q1 VUE	0.828	Almost Perfect	0.242	Fair	0.234	Fair
Q2 VUE	0.712	Substantial	0.571	Moderate	0.526	Moderate
Q3 VUE	0.298	Fair	0.013	Slight	1.00	Perfect
Q4 VUE	0.336	Fair	0.828	Almost Perfect	0.4	Fair
Q5 VUE	0.439	Moderate	0.268	Fair	0.231	Fair
Q6 VUE	0.545	Moderate	0.268	Fair	-0.119	Less than chance

Table 12. (Continued) Kappa Statistics for Intra-observer variability (VUE images)

Inter-observer variability was characterized between the three radiologists that participated in the experiment. This variation between radiologists is also accounted for in the Bayesian Hierarchical model, and is shown visually Figure 15.
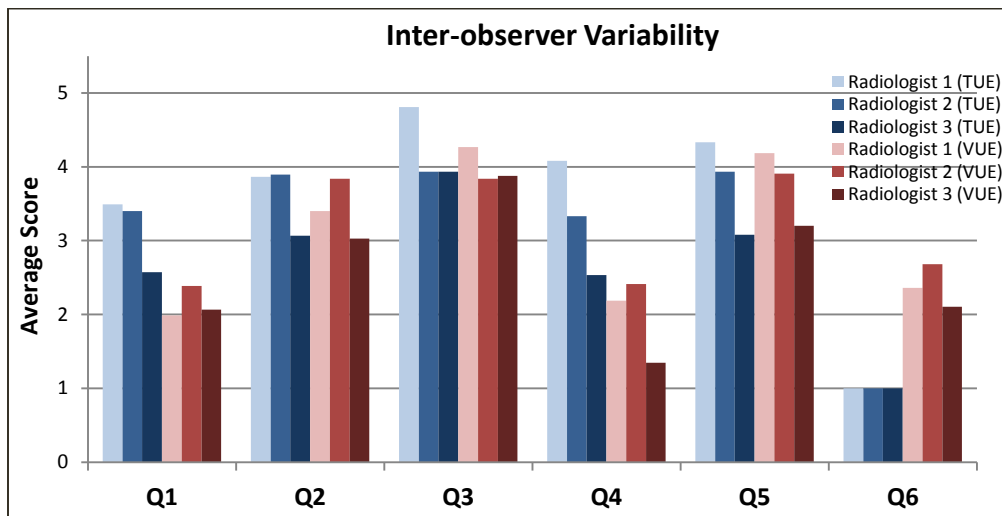
Figure 15. Inter-observer variability between Radiologists

4.1.2 Discussion: Sub Aim 1.1

The Likert scale for each question presented to each radiologist was discrete in increments of 1 point. As a result of the discrete nature of the scale, the VUE images were considered to be non-inferior to TUE images if the difference in answers for each question was within -0.5 points or greater. This accounted for circumstances in which a radiologist may have felt the appropriate response to a given question was, for example 3.5, yet had to choose either 3 or 4 as the answer, which is a departure of 0.5 from the true perceived difference. The ability to recognize an image as TUE or VUE may have influenced the decision, in this example, to choose 3 or 4. Therefore, the -0.5 threshold was used to control for any potential bias.

The results of this study are summarized in Table 13, where β represents the mean difference between VUE and TUE images calculated using the Bayesian Hierarchical model. Recall that this model took into account several factors of variability associated with the study, and is therefore not a raw mean difference.

Question	*Results*
1. Visualization of major vessels	Uncertain ($\beta = -0.514$)
2. Visually sharp reproduction of pancreatic contour	Non-inferior ($\beta = -0.092$)
3. Visualization of calcifications	Non-inferior ($\beta = -0.127$)
4. Depiction of liver parenchyma	Inferior ($\beta = -0.682$)
5. Visualization of adrenal glands	Non-inferior ($\beta = -0.013$)
6. Corticomedullary Differentiation	Non-inferior ($\beta = 1.379$)

Table 13. Qualitative Study Results Summary

In the Bayesian Hierarchical model the variation was calculated to be $\sigma = 0.563$ for inter-observer variability and $\sigma = 0.370$ for intra-observer variability. Given that the threshold was chosen to be -0.5, it can be seen that these resulting variations are substantial, indicating the

necessity for a Bayesian Hierarchical model as opposed to simply using a paired t-test. Notice that if the conventional t-test had been used to evaluate these data, these variations would not be accounted for and the associated uncertainty with each result would be substantially greater. A detailed discussion for the results from each question is given below.

Question 1, evaluating the visualization of major vessels, resulted in statistical uncertainty regarding the difference between VUE and TUE image scores (β = -0.514). This is because the 95% credible interval (-0.624, -0.408) contained the -0.5 threshold for differentiation; therefore, the difference could be attributed to the limited data set acquired as reflected by the standard deviation. The acquired data set could be increased, which would result in a decrease of the standard deviation, until the 95% CI no longer contained the -0.5 threshold. In this case, a definitive statistical result could be obtained. However, statistical uncertainty implies clinical inferiority. An example comparison of the appearance of the hepatic vein in TUE and VUE images is provided in Figure 16. The algorithm used to reconstruct VUE images functions by estimating the volume of iodine in each voxel and replacing it with an equivalent volume of blood [27]; therefore, the visualization of vessels should theoretically be identical for TUE and VUE images. As can be seen in Figure 16, this is not the case and the hepatic veins are more clearly visible in the TUE image. This is possibly due to inaccurate removal of iodine signal from the image or perhaps differences in the levels of iterative reconstruction applied to TUE and VUE images. It was noted by each radiologist that visualization of arteries was good, but visualization of veins was poor in VUE images.
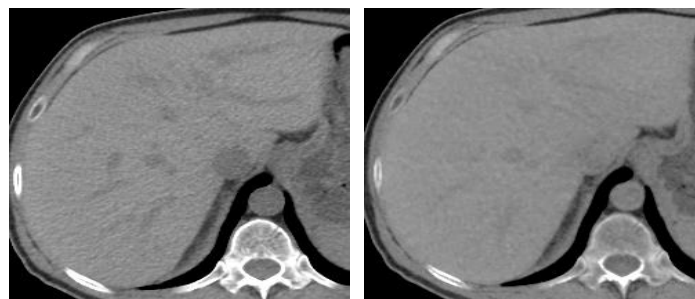
Figure 16. Appearance of hepatic veins in TUE (left) and VUE (right) images

The greatest (negative) difference between scores for VUE and TUE images was for the depiction of liver parenchyma ($\beta = -0.682$). This is potentially a result of the variation in reconstruction techniques used for the TUE and VUE images, as described previously. A common complaint among radiologists when answering this question was that the VUE images were "grainy" and "noisy". Iterative reconstruction applied to TUE images but not VUE images likely reduced noise and the visual appearance of "graininess", which was more appealing to the radiologists. This motivated the addition of the third specific aim of the project, which quantitatively assesses the impact of varying levels of ASIR on enhancement accuracy in VUE images.

Question 6, concerning corticomedullary differentiation yielded the greatest absolute difference between VUE and TUE images ($\beta = 1.379$), but in for this question VUE images were scored greater than or equal to TUE images in all cases. All TUE images were given a score of 1, indicating no corticomedullary differentiation, and scores for VUE images ranged from 2-3, indicating that there were either slight (2) or extreme (3) differentiation. Corticomedullary differentiation typically occurs during the corticomedullary phase of renal enhancement, and is a physiologic process that is observed when there is contrast within the cortex that has not yet reached the medulla. The corticomedullary differentiation observed in VUE images was a result of the MSI algorithm inaccurately removing the substantial amounts of iodine signal present in the post-contrast DECT images, which were acquired during the corticomedullary phase of enhancement. This differentiation in VUE images is visible even to the untrained eye (Figure 17), and is an artifact of the MSI algorithm. Although VUE images were scored higher than TUE images, it should be noted that this result implies that VUE images differ from reality (i.e. TUE images) where this differentiation is not observed because there is not yet any iodine contrast in the cortex. Corticomedullary differentiation could potentially be minimized or eliminated by changing the phase in which the DECT data are acquired [43], e.g. by further delaying the post-

contrast injection scan time and acquiring the DECT data in the nephrographic phase when renal enhancement is relatively uniform.
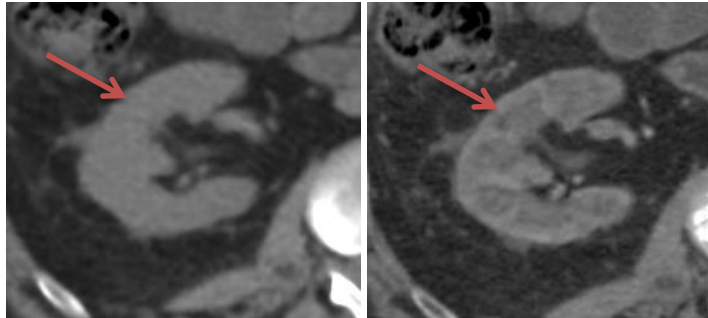
Figure 17. Corticomedullary differentiation in TUE (left) and VUE (right) images

The differences between scores for VUE and TUE images for the reproduction of the pancreatic contour (β = -0.092) and the visualization of adrenal glands (β = -0.013) were not statistically significant. The mean difference in scores, represented by β, between TUE and VUE images was minimal. It was expected that the pancreas and adrenal glands would not be affected by the MSI algorithm because each does not uptake a significant amount of iodine contrast. Given the physiological nature of the pancreas and adrenal glands and considering the vascularity of each, it was expected that the scores would not significantly differ between TUE and VUE images, and this was experimentally proven to be true.

Although the results for the visualization of calcifications (β = -0.127) indicated that VUE images were non-inferior to TUE images, this result is misleading. It was noted that each radiologist at least once during the study suggested that the scoring for calcifications was in essence binary, i.e. it is seen or not seen. There were cases in which calcifications were seen in TUE images and not VUE images, and some cases for which the opposite was true (Table 14). The few cases where calcifications were seen in VUE but not TUE images is likely attributable to the variability of the observer between scoring the TUE and corresponding VUE image independently. However, there are more instances where calcifications were seen in TUE images and not TUE images. This result is consistent with other studies, and has been referred to in the

43

literature as the "subtraction artifact" [9]. The subtraction artifact is a result of the inability of the algorithm to accurately distinguish iodine from other materials with high atomic numbers, such as calcium. The multi-material decomposition method presumably decomposes a voxel into only two materials [7], such as water and iodine, which results in all materials contained in a given voxel being represented as some weighted combination of water and iodine. Since calcium has a large photoelectric cross-section, a voxel with calcium will be assigned by the algorithm as containing some percentage of iodine, which is subtracted when the VUE image is reconstructed. This is apparent is a case where calcifications are not as bright in the VUE as in the TUE, or when they are not seen at all, as well as when visually comparing the appearance of the spine between VUE and TUE images.

	Number of instances calcifications were seen in TUE but not VUE	Number of instances calcifications were seen in VUE but not TUE	
Radiologist 1	7	1	
Radiologist 2	12	2	
Radiologist 3	11	4	
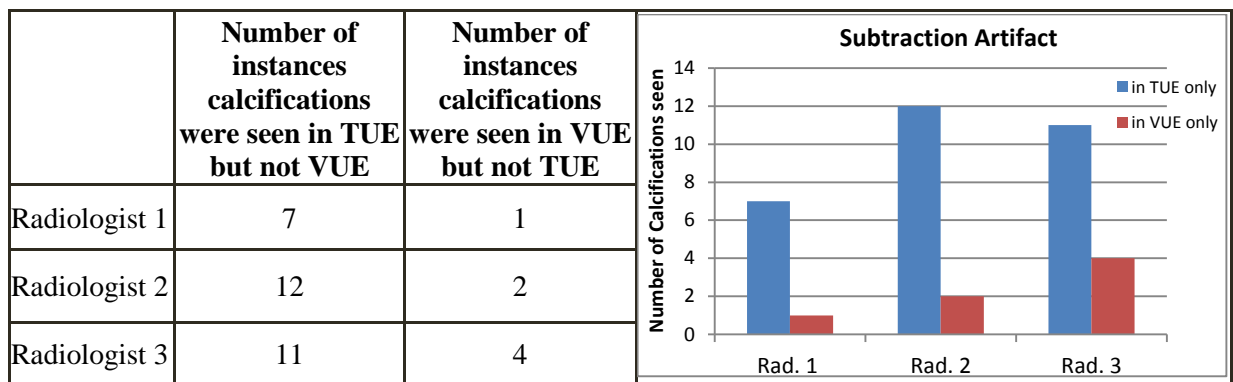
Table 14. Comparison of instances in which calcifications were not seen in one of the images

Although there were cases where calcifications were seen in VUE but not TUE, this occurred much less often than visualization in TUE but not VUE. When considering these cases of visualization in VUE but not TUE one should consider the large variations calculated in the mixed effects analysis for inter- and intra-observer variability ($\sigma = 0.563$ and 0.370, respectively). However, the number of instances where calcifications were seen in TUE but not VUE is substantial, even considering these sources of variation, and is likely not attributable to these sources of variability. This result instead likely reflects an artifact of the algorithm, which subtracts calcium signal due to the representation of calcium as a weighted combination of water and iodine.

4.1.3 Results: Sub Aim 1.2

The quantitative study was based on CT number measurements in the patient exams used in the qualitative study. A plot of the average CT number measured in each region of interest can be found in Figure 18, and the corresponding quantitative comparison can be found in Table 15.
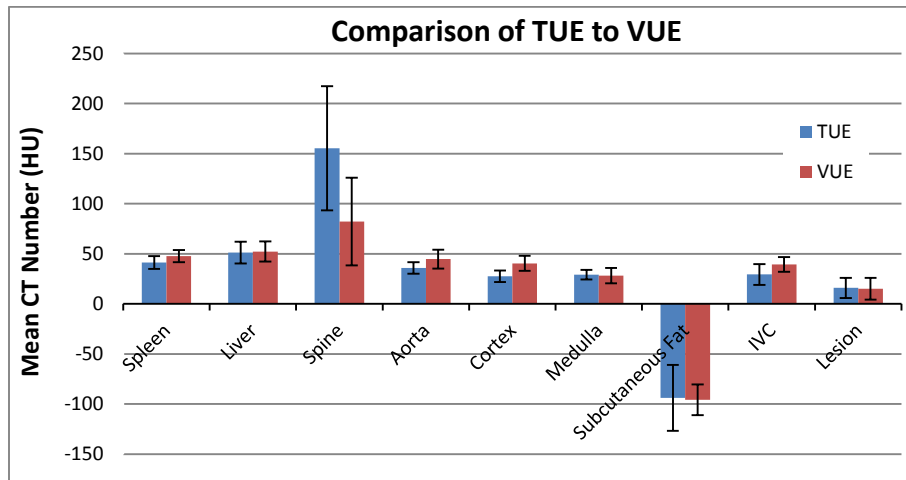
Figure 18. Comparison of average HU measured in TUE vs. VUE

	TUE Mean CT number (HU)	VUE Mean CT number (HU)
Spleen	41.4	47.6
Liver	51.2	52.3
Spine	155.3	82.2
Aorta	35.9	44.8
Cortex	27.5	40.4
Medulla	29.1	28.1
Subcutaneous Fat	-99.2	-95.6
IVC	29.4	39.2
Cystic Lesion	16.0	15.1

Table 15. Quantitative results: Average CT numbers

The fraction of cases where the absolute difference between TUE and VUE measurements was greater than 10 HU was plotted to visualize where the greatest differences occurred, as shown in Figure 19.
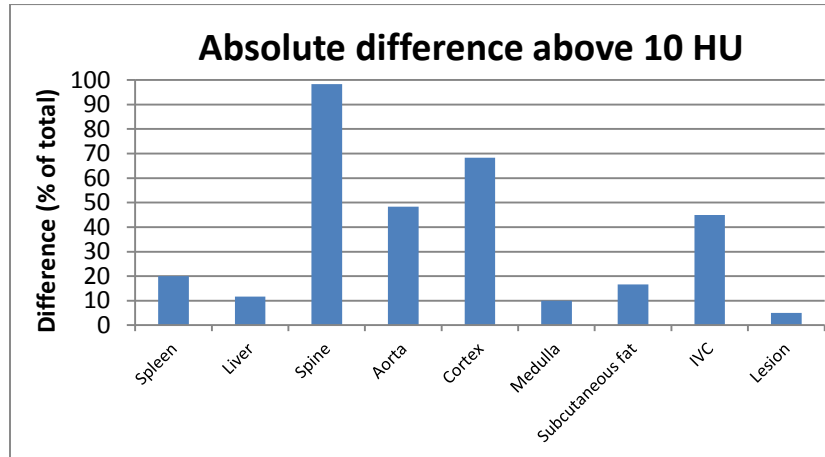
Figure 19. Absolute difference in CT number between TUE and VUE images

The data collected from this study were analyzed using a student's paired t-test. The ± 6 HU tolerance at 120 kVp for water required by the manufacture for the 750HD DECT scanner was used as the basis for the determination of a relative threshold. The ± 6 HU tolerance was converted into an uncertainty about the linear attenuation coefficient of water at 70 keV:

$$\mu = 0.1948 \pm 0.0012 \; ^{cm^2}/_g \qquad \text{Equation 4.1.3-1}$$

This equates to a tolerance of ± 0.6% about water. The average CT number measured on the TUE images for each area of interest was converted to a linear attenuation coefficient, and a ± 0.6% threshold was calculated about each. The average of the upper and lower tolerances (i.e. -0.6% and +0.6%) was calculated, converted back to CT number (HU) and used as the threshold for each organ. The thresholds used for the t-test are given in Table 16.

	Mean CT number (HU)	μ (cm^{-1})	0.6% tolerance in μ (cm^{-1})	$\pm$ HU
Spleen	41.4	0.203	0.0012	6.25
Liver	51.2	0.205	0.0012	6.31
Spine	155.3	0.225	0.0014	6.93
Aorta	35.9	0.202	0.0012	6.22
Cortex	27.5	0.200	0.0012	6.16
Medulla	29.1	0.201	0.0012	6.17
Fat	-99.2	0.176	0.0011	5.41
IVC	29.4	0.201	0.0012	6.18

Table 16. Determination of Threshold of differentiation

The results of this study are summarized in Table 17 below. A p-value of < 0.05 indicated that VUE images were non-inferior to TUE images, and was calculated based on the threshold determined for each area of interest. A p-value of ≥ 0.05 indicated that VUE images were inferior to TUE images.

Organ	*P-value*	*95% CI for the difference*	*Results*
Spleen	0.815	(-7.53, -5.01)	Inferior
Liver	< 0.001	(-0.85, 3.05)	Non-inferior
Spine	1.000	(64.12, 82.23)	Inferior
Aorta	0.999	(6.57, 11.13)	Inferior
Cortex	1.000	(10.69, 15.25)	Inferior
Medulla	< 0.001	(-0.82, 2.86)	Non-inferior
Subcutaneous Fat	0.676	(1.71, 5.11)	Inferior
Inferior Vena Cava	0.999	(-7.42, 12.24)	Inferior

Table 17. Quantitative results summary

4.1.4 Discussion: Sub Aim 1.2

The thresholds used for statistical analysis were based on physics principals, and therefore leave open the question of the clinical relevance of the results. Consider, for example, the results for the spleen (based on a ± 6.25 HU threshold). The t-test indicated that VUE images are inferior to TUE images, but the 95% confidence interval (CI) indicates that VUE images will measure within -7.53 HU of TUE images. To assess the clinical relevance of these results, an evaluation of the implications of the variation in CT number on a grayscale image was conducted. The purpose of this assessment was to determine if the variation in CT number between TUE and VUE images, based on the calculated 95% CI, would even be perceivable to a radiologist.

The evaluation was done for a window width/ window level (WW/WL) of 500/50, which is a common default setting for abdominal image viewing. For an image displayed on a 10 bit monitor 1,024 grayscales are available which equates to approximately 2 gray levels per HU. If it is assumed that the human eye can perceive between 64-128 shades of gray, then a change in every 4-8 HU would be perceived by the human observer. Referring to Table 17, the 95% CI for the spleen and subcutaneous fat indicate that there is likely no clinical significance to these results and that from a clinical perspective measurements for the spleen and fat for VUE images are not inferior to TUE images.

Figure 20 demonstrates differences in the appearance of bone between TUE and VUE images. Notice that the spine appears much brighter in the TUE image, which could be a consequence of the inability of the material suppression algorithm to accurately distinguish bone from an iodine-blood mixture. This has been referred to in the literature as a "subtraction artifact" [9]. For this feasibility study, the subtraction of calcium signal in the spine is likely irrelevant for assessment of renal masses.
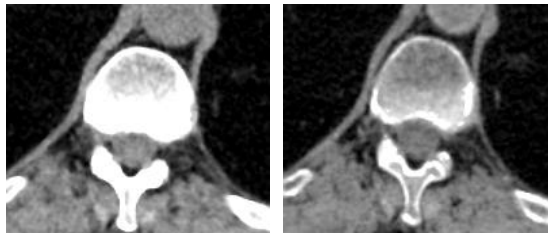
Figure 20. Comparison of spine appearance in TUE (left) to VUE (right)

4.1.5 Dose Considerations

The volume computed tomography dose index ($CTDI_{vol}$) was recorded from the dose report for each patient exam. The average $CTDI_{vol}$ for the pre-contrast phase (TUE) well as for the total CT exam are given in Table 18. Note that the reduction (%) is representative of the particular exam protocol used for patients in the retrospective study, which involves acquisition of multiple post contrast images. For renal protocols, which typically involve the acquisition of fewer post-contrast images, the reduction in $CTDI_{vol}$ (%) resulting from elimination of the pre-contrast phase would be a larger fraction of the total.

Mean Values	Total Number (N)	Age (years)	Weight (kg)	BSA (m^2)	$CTDI_{vol}$ for TUE (mGy)	Total $CTDI_{vol}$ (mGy)	Reduction (%)
Women	27	62.3	70.8	1.96	11.0	113.8	9.7
Men	33	62.0	67.9	1.94	10.8	127.7	8.5
Overall	60	62.1	74.6	1.90	10.5	121.5	8.7

Table 18. Estimated doses from the pre-contrast images for patient exams

4.1.6 Limitations of the retrospective study

The raw CT data for the patient exams used in this study were no longer available; therefore the TUE and VUE images could not be reconstructed using identical techniques. The TUE images were reconstructed with 60% ASIR and the SOFT reconstruction filter, whereas the DECT data used to reconstruct VUE images were reconstructed with 0% ASIR and the STANDARD reconstruction filter.

4.2 Specific Aim 2

4.2.1 Technical Notes

4.2.1.1 Results and discussion: Iodine concentration determination

CT numbers were measured for each Optiray-water mixture and plotted to determine a relationship between CT number and iodine concentration. The results were plotted and linear regression was used to estimate a relationship between CT number and iodine concentration, as shown in Figure 21. The CT numbers predicted from previous experiments [38] are plotted alongside the CT numbers measured in this experiment. The relationship between CT number and iodine concentration was determined to be:

$$Iodine\ concentration\ \left(\frac{mg}{mL}\right) = 0.0501 * (CT\ number) - 1.08 \quad\quad Equation\ 4.2.1.1 - 1$$
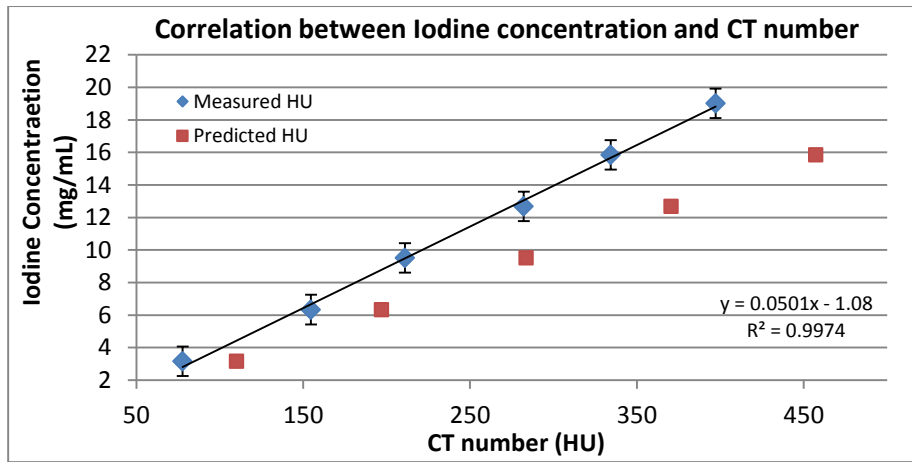
Figure 21. Correlation between iodine concentration (mg/mL) and CT number (HU)

The variation between predicted CT number from previous experimentation and the measured data is likely reflective of the variation between energy spectra from CT scanner to CT scanner.

4.2.1.2 Results and discussion: Phantom set-up verification

        VUE images were reconstructed from DECT imaging of the Jaszczak phantom. The results of the experiment for the 31.8 mm diameter sphere (sphere 1) are plotted in Figure 22, and Figure 23 for the 25.4 mm sphere (sphere 2). The results of the Jaszczak phantom study indicate that the output of the MSI algorithm for VUE image reconstruction is substantially the same in both in positive and negative contrast backgrounds. Encouraged by these results, we proceeded with Sub Aim 2.2 of the phantom study.
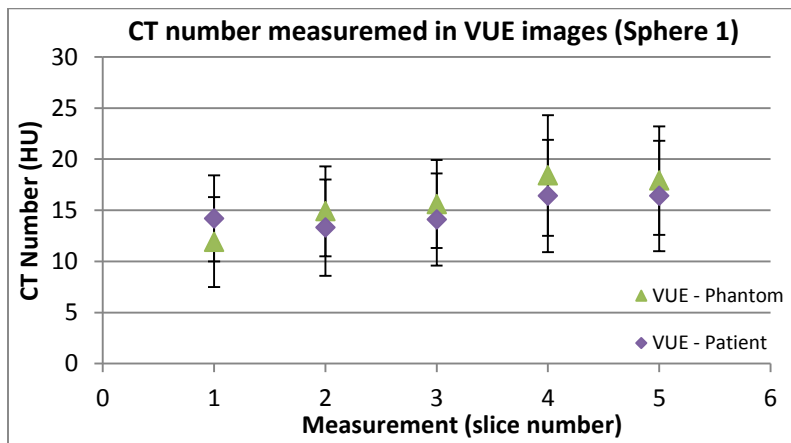
Figure 22. Positive versus negative contrast comparison for Sphere 1
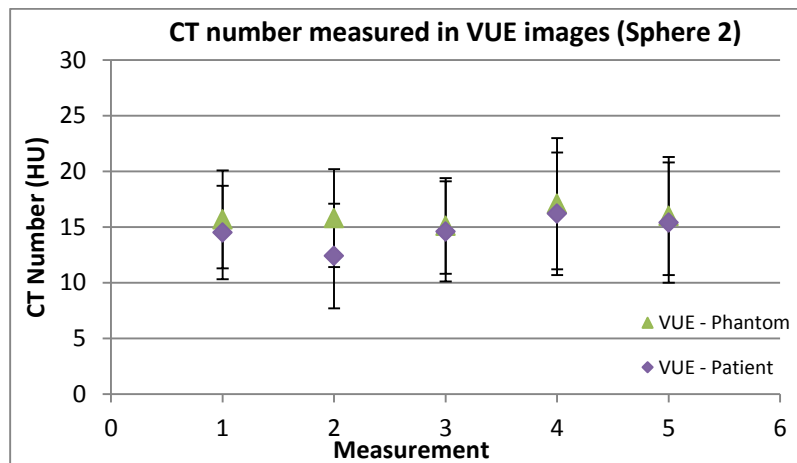
Figure 23. Positive versus negative contrast comparison for Sphere 2

4.2.2 Results: Sub Aim 2.2

The measured CT number and noise for each preset imaged with the medium phantom can be seen in Figures 24 and 25, respectively. Four GSI protocols were selected for imaging the small and medium phantom sizes, and four protocols were selected for imaging the large phantom.
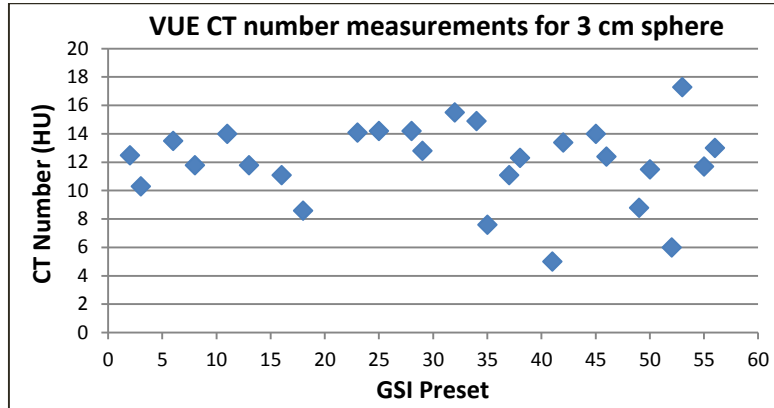
Figure 24. VUE CT number measurements for each GSI protocol
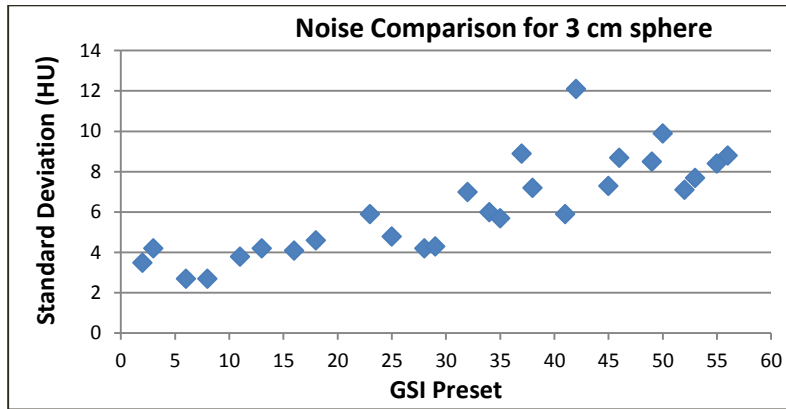
Figure 25. VUE image noise measurements for each GSI protocol

The protocols selected for use in Sub Aim 2.2 are listed in Table 19. GSI preset 10 was selected for imaging all three phantoms to bridge the gap between clinical practices and the retrospective study for further investigation of other presets in the phantom study. Preset 10 was used in image acquisition of almost all patient cases in the retrospective study independent of patient size.

	GSI Preset	Bowtie	Beam Width (mm)	Rotation Time (s)	mA	CTDI$_{vol}$ (pitch 0.969)
Used for small and medium phantoms	10	Large	40	0.8	600	25.5
	11	Medium	40	0.8	600	26.7
	16	Medium	40	0.6	640	22.9
	29	Medium	20	0.8	550	27.6
Used for large phantom	36	Large	40	0.8	360	10.3
	10	Large	40	0.8	600	25.5
	12	Large	20	0.8	600	28.2
	22	Large	40	0.7	375	10.8

Table 19. Selected GSI presets

4.2.3 Discussion: Sub Aim 2.2

It was difficult to assess the accuracy of VUE image CT numbers compared to the TUE image baseline, which was acquired with water in the phantom inserts. Recall that the MSI algorithm used to reconstruct VUE images subtracts the iodine concentration contained within each voxel and replaces it with an equivalent volume of blood [27]. As a result, the TUE images acquired with water in the spheres will not be representative of what is expected from the VUE images, which would in theory be a blood-water mixture after the iodine replacement. The TUE images used in the experiment with water filled spheres provided a baseline measurement of approximately 0 HU, whereas the VUE images resulted in an average measurement of 13 HU for the 3 cm sphere.

An experiment was conducted in an attempt to estimate the expected baseline VUE measurement that could be used for comparison of GSI protocols. Mixtures of water and iodine were prepared with increasing iodine concentrations, and CT numbers were measured in the resulting VUE images. CT number (HU) was plotted against iodine concentration (mg/mL) and

the relationship was extrapolated to zero to estimate what the expected CT number would be for 0 mg/mL iodine concentration, which resulted in an expected baseline VUE measurement of 14.7 HU. The prominent issue with this method was that a GSI protocol had to be selected in order to acquire DECT datasets for VUE image reconstruction; therefore, the results are inherently biased toward that protocol. Since the goal of this Sub Aim is to select the top candidate protocols, this is problematic. As a result, four GSI candidate protocols were selected by careful evaluation of the full protocols list, taking into consideration measured image noise and the specific technique parameters.

The GSI protocols were selected to allow for variation in CT acquisition parameters between protocols, as well as with consideration to the amount of noise measured from each. For the medium and small phantoms (refer to Table 19):

- GSI 10 selected because of common clinical use
- GSI 10 → GSI 11 variation in bowtie filter
- GSI 11 → GSI 16 variation in rotation time and mA
- GSI 16 → GSI 29 variation in beam width

For the large phantom (refer to Table 19):

- GSI 10 selected because of common clinical use
- GSI 36 → GSI 10 variation in mA, mAs, and $CTDI_{vol}$
- GSI 10 → GSI 12 variation in beam width
- GSI 12 → GSI 22 variation in rotation time and mA

Example images acquired using each selected preset at the same location in the small phantom with 5.00 mm thickness are shown in Figure 26, and example images of each preset selected for the large phantom are shown in Figure 27.
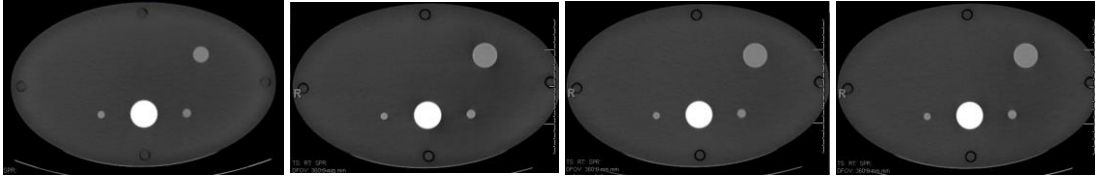
Figure 26. Example images of the medium phantom for the selected GSI presets (from left to right) GSI 10, 11, 16, and 29
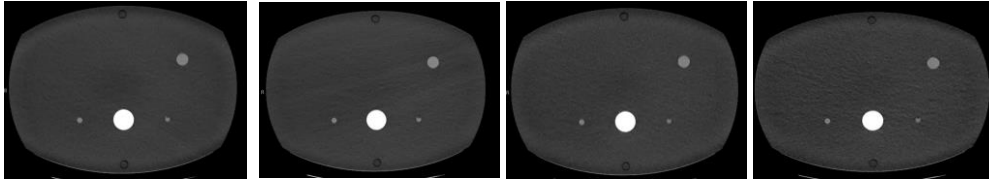
Figure 27. Example images of the large phantom for the selected GSI presets (from left to right) GSI 10, 12, 22, and 36

Limitations of Sub Aim 2.2

In order to make a more accurate comparison of the performance of each GSI protocol in relation to the expected TUE measurement, the experiment would need to be conducted with blood only for TUE image acquisition, and a blood-iodine mixture for DECT image acquisition. This would allow for reconstruction of VUE images expected to have CT number similar to the TUE images, considering the nature of the MSI algorithm. Using blood would allow for an assessment of the variation of CT numbers for all GSI protocols to TUE image CT numbers.

4.2.4 Results: Sub Aim 2.3

A Bayesian Hierarchical model was used to analyze all phantom data. This method was chosen because. This model was chosen to allow for direct quantification of uncertainty resulting from many parameters in the study, including variation in lesion size, patient size, enhancement, etc. Note that the error bars for each graph in the subsequent sections represent $\pm \sigma_{total}$ (equation 3.2.4-2). Additional graphs for each section can be found in Appendix 6.6.

<u>Scenario 1</u>

Each phantom was imaged in varying configurations for a baseline CT number of -100 HU, simulated with vegetable oil in the inserts. Because there was no enhancement for this scenario, a direct comparison was made for VUE vs. TUE CT number measurements. Graphs of varying parameters can be seen in Figures 28 and in Appendix 6.6. The results of the Bayesian Hierarchical model for comparison of VUE techniques to TUE images are quantitatively summarized in Table 20 in the following section.
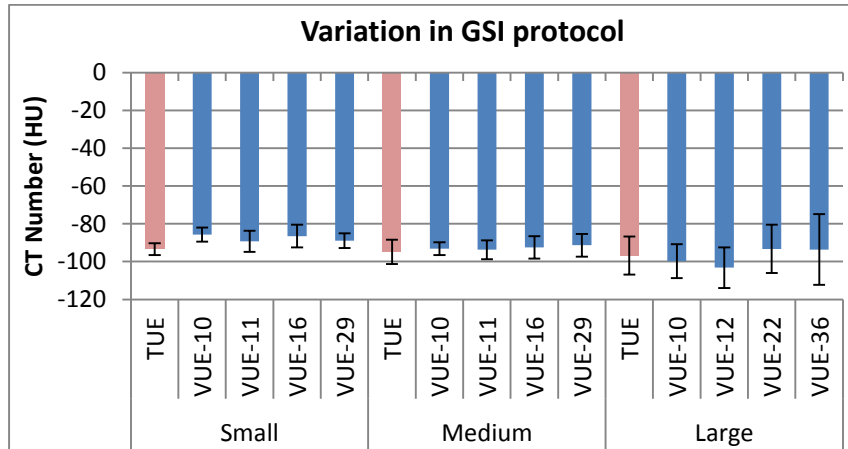
Figure 28. Evaluation of the impact of GSI protocol on CT number in VUE vs. TUE images. Plotted data represent the 1 cm sphere in the center of the FOV.

Scenario 2

Each phantom was imaged in varying configurations for a baseline CT number of
0 HU, simulated with distilled water in the inserts. Because there was no enhancement for this
scenario, a direct comparison was made for VUE vs. TUE CT number measurements.
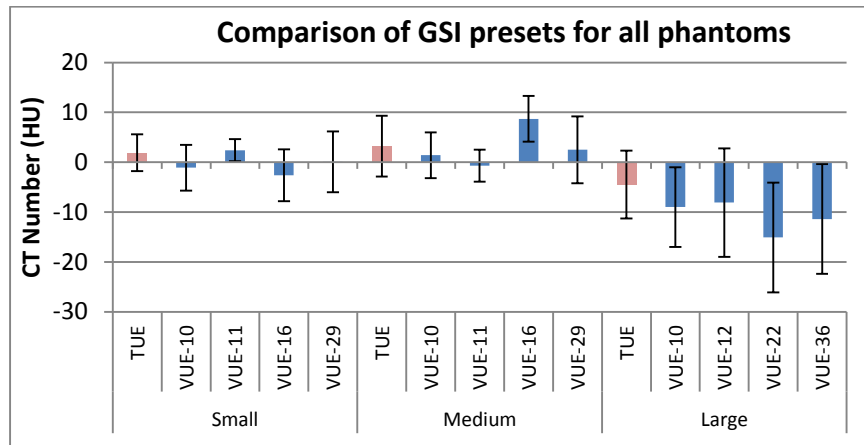
**Figure 29. Comparison of each GSI preset to TUE CT number measurements for the 1 cm
lesion size located in the center of the SFOV.**

For scenarios 1 and 2, the TUE and VUE CT number measurements were directly
compared, because there was no enhancement in post-contrast images. As a result, a single model
was used for statistical analysis of these scenarios. Table 20 quantitatively represents the results
of each GSI protocol as compared to the TUE image measurements. Note that the results are
given as the difference between each VUE protocol as compared to the TUE measurements,
taking into account uncertainties from each variable. The posterior probability can be interpreted
as:

- Posterior probability > 0.95 implies significant positive variation of VUE images

- Posterior probability < 0.05 implies significant negative variation of VUE images

- Posterior probability = 0.5 implies no significant difference between VUE and TUE
  images

The results from the Bayesian Hierarchical model, shown in Table 20, indicate that there is no statistically significant variation between each VUE protocol and the TUE images across a wide range of varying parameters (including lesion size and position of the lesion within the field of view) for simulated angiomyolipoma and benign cystic lesions. The parameter $\sigma_{Protocol}$ given in Table 20 represents the standard deviation in CT number measurements resulting from differences in GSI protocol, as computed by the Bayesian Hierarchical model.

	Small Phantom		Medium Phantom		Large Phantom	
	95% CI for difference	Posterior Probability	95% CI for difference	Posterior Probability	95% CI for difference	Posterior Probability
VUE-10 [10]	(-1.437, 2.380)	0.564	(-2.111, 1.838)	0.502	(-10.246, 1.006)	0.238
VUE-11 [12]	(-1.297, 2.434)	0.555	(-1.786, 2.239)	0.515	(-9.990, 1.026)	0.25
VUE-16 [22]	(-1.441, 2.704)	0.56	(-1.252, 2.973)	0.56	(-11.138, 0.916)	0.226
VUE-29 [36]	(-1.595, 2.148)	0.524	(-1.584, 2.360)	0.531	(-8.871, 1.353)	0.273
$\sigma_{Protocol}$	(0.029, 2.388)	--	(0.029, 2.582)	--	(0.037, 7.302)	--

Table 20. Bayesian Hierarchical Model results for scenarios 1 and 2. The presets in brackets are those used for the large phantom.

Scenario 3

For Scenarios 3-5, the enhancement values of interest will be labeled as follows in each of the graphs:

$$\textit{VUE image based enhancement}: \Delta VUE = DECT_{post-contrast} - VUE$$

$$\textit{TUE image based enhancement}: \Delta TUE = SECT_{post-contrast} - TUE$$

The error bars in graphs shown in Scenarios 3-5 represent $\pm\ \sigma_{total}$ (as described in section 3.2.4), where the term for standard deviation within each ROI measurement (σ_N) was added in quadrature for pre- and post-contrast measurements to estimate the error for enhancement.

Each phantom was imaged in varying configurations for a baseline CT number of 20 HU, simulated with an apple juice and distilled water mixture in the inserts. For this scenario two cases were simulated to mimic low and intermediate enhancement. Recall that one solution was made and used for all variation in phantom configuration, including phantom size. As can be seen in Figure 30, the same solution measured different CT numbers across patient size. This variation in measured enhancement across patient size is not problematic because the same solution was used to acquire SECT and DECT post-contrast images for each phantom, which is the comparison of interest for this study.

Figure 30. Scenario 3: Comparison of enhancement with TUE vs. VUE as the baseline image for varying patient size, enhancement, and GSI presets for the 3 cm sphere located in the periphery of the SFOV

Scenario 3 was unique from all other scenarios because a baseline value of 20 HU was simulated. As a result, an individual Bayesian Hierarchical model was used to fit the data for this scenario to most effectively quantify the uncertainties and determine the posterior probability. The results are given as the difference between enhancement values for each GSI protocol as the baseline image compared to measurements with TUE images as the baseline, taking into account uncertainty

59

resulting from each parameter. As previously stated the posterior probability can be interpreted as:

- Posterior probability > 0.95 implies significant positive variation of VUE images

- Posterior probability < 0.05 implies significant negative variation of VUE images

- Posterior probability = 0.5 implies no significant difference between VUE and TUE images

The results from the Bayesian Hierarchical model, shown in Table 21, indicate that there are significant differences between each enhancement from each VUE protocol and the TUE images across a wide range of varying parameters (including lesion size and position of the lesion within the field of view) for simulation of Bosniak category II-IIF lesions. The 95% credible interval is representative of the difference in enhancement values from each GSI protocol to the TUE images, which is significant. This is also demonstrated visually in Figure 30.

	Small Phantom		Medium Phantom		Large Phantom	
	95% CI for difference	Posterior probability	95% CI for difference	Posterior probability	95% CI for difference	Posterior probability
VUE-10 [10]	(-18.312, -14.531)	0	(-15.565, -12.176)	0	(-10.263, -4.618)	0
VUE-11 [12]	(-18.339, -14.574)	0	(-15.948, -12.570)	0	(-9.650, -3.942)	0
VUE-16 [22]	(-18.458, -14.613)	0	(-15.783, -12.370)	0	(-11.324, -5.851)	0
VUE-29 [36]	(-18.106, -14.423)	0	(-16.008, -12.634)	0	(-10.238, -4.622)	0
$\sigma_{Protocol}$	(4.359, 21.15)	--	(3.759, 18.258)	--	(1.954, 10.482)	--

Table 21. Bayesian Hierarchical Model results for scenario 3. The presets in brackets are those used for the large phantom.

Each phantom was imaged under varying configurations for a baseline CT number of 40 HU simulated with an apple juice and distilled water mixture in the inserts. For this scenario low enhancement (5-10 HU) and intermediate (15- 20 HU) enhancement cases were simulated. Graphs of different parameters can be seen in Figure 31 and in Appendix 6.6.
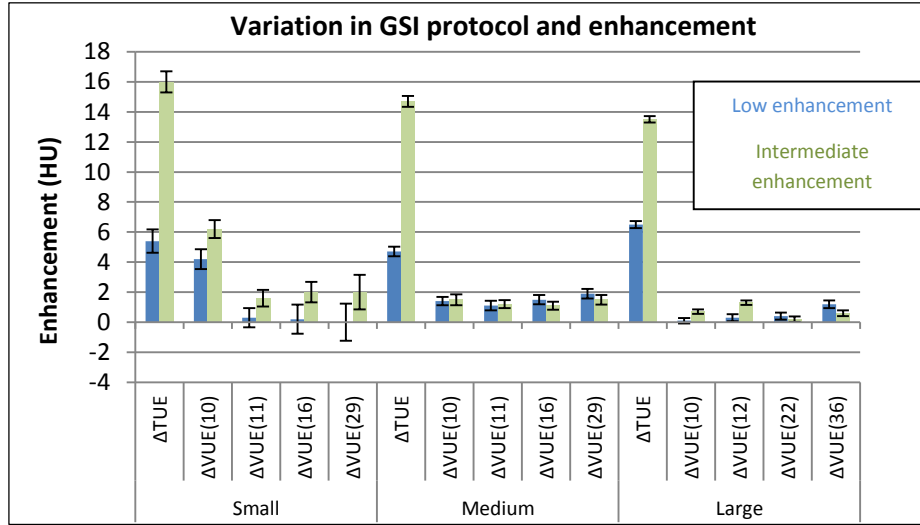
Figure 31. Scenario 4: Comparison of enhancement with TUE vs. VUE as the baseline image for varying patient size, iodine concentrations, and GSI presets for the 3 cm sphere located in the periphery of the SFOV

Scenarios 4 and 5 simulated as baseline lesion measuring 40 HU, and then varying enhancement situations were simulated. Consequently, a separate Bayesian Hierarchical model was used to fit this data, and is shown in Table 22.

Scenario 5

Each phantom was imaged under varying configurations for a baseline CT number of 40 HU simulated with an apple juice and distilled water mixture in the inserts. For this scenario only high enhancement (40 HU) was simulated to mimic a Bosniak category IV lesion that is clearly malignant. Figure 32 shows a comparison of enhancement measurements with each GSI protocol used as the baseline for calculation compared to TUE baseline measurements.

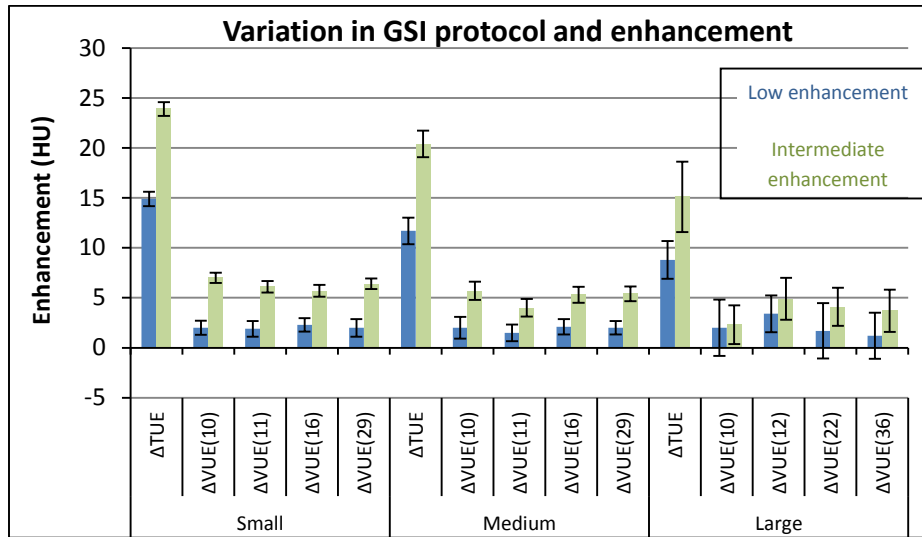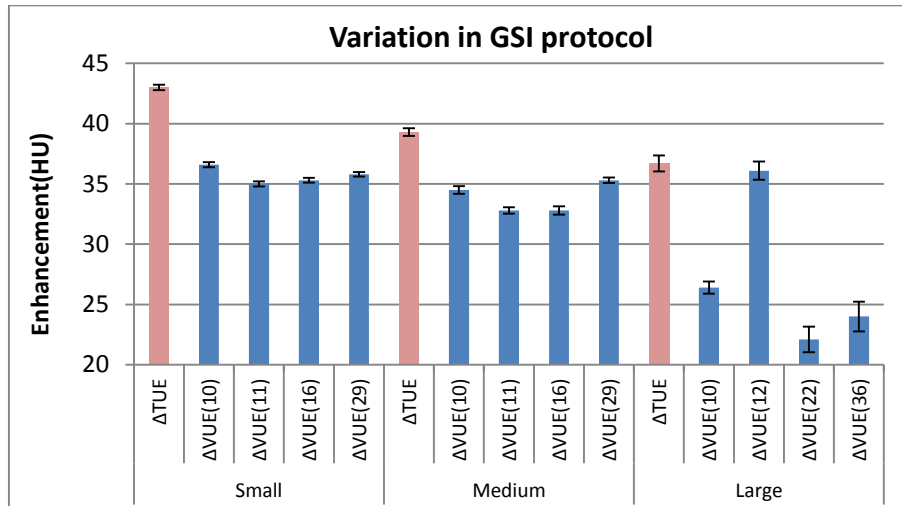**Figure 32. Scenario 5: Comparison of enhancement with TUE vs. VUE as the baseline image for varying patient size and GSI presets for the 3 cm sphere located in the periphery of the SFOV**

The results from the Bayesian Hierarchical model, shown in Table 22, indicate that there are significant differences between enhancement measurements for each baseline VUE image and the TUE images across a wide range of varying parameters (including lesion size and position of the lesion within the field of view). The 95% credible interval is representative of the difference in enhancement values from each GSI protocol to the TUE images, for which significance is demonstrated by a posterior probability of 0 for all protocols across all phantom sizes. This is also demonstrated visually in Figure 31. The parameter $\sigma_{Protocol}$ is the variation between enhancement

for all VUE and TUE image based measurements, as calculated from the Bayesian Hierarchical model.

	Small Phantom		Medium Phantom		Large Phantom	
	95% CI for difference	Posterior probability	95% CI for difference	Posterior probability	95% CI for difference	Posterior probability
VUE-10 [10]	(-10.469, -5.940)	0	(-12.028, -5.740)	0	(-13.234, -6.247)	0
VUE-11 [12]	(-12.113, -7.324)	0	(-13.123, -6.705)	0	(-11.166, -4.593)	0
VUE-16 [22]	(-11.791, -7.013)	0	(-12.918, -6.201)	0	(-14.340, -7.332)	0
VUE-29 [36]	(-11.417, -6.491)	0	(-12.168, -5.508)	0	(-11.608, -5.021)	0
$\sigma_{Protocol}$	(2.386, 12.267)	--	(2.402, 12.672)	--	(2.384, 12.862)	--

Table 22. Bayesian Hierarchical Model results for scenario 3. The presets in brackets are those used for the large phantom.

Position of the simulated lesion within the field of view was varied between the center and periphery locations of the phantom, as shown in Figure 7. The standard deviation resulting from position of the lesion within the FOV was estimated using probabilities from the Bayesian Hierarchical model. The deviation, σ_{FOV}, is shown in Table 23. The posterior probabilities calculated from the Bayesian Hierarchical model indicate significant differences in CT number (scenarios I and II) and enhancement (scenarios III-V) measurements resulting from different locations within the FOV in VUE enhancement measurements for all scenarios. Previous studies have also found that the material decomposition function of GSI using a GE CT750 HD scanner is dependent on position within the FOV for varying iodine concentrations, and may be attributable to beam hardening in FOV locations where CT number uncertainty was high [44].

Scenario	Small Phantom		Medium Phantom		Large Phantom	
	95% CI for variation (σ_{FOV})	Ext Val	95% CI for variation	Ext Val	95% CI for variation (σ_{FOV})	Ext Val
I - II	(0.055, 8.099)	1	(0.031, 2.587)	1	(0.063, 8.139)	1
III	(0.074, 1.994)	1	(0.061, 1.793)	1	(0.033, 2.437)	1
IV - V	(0.031, 2.170)	1	(0.033, 3.343)	1	(0.070, 3.928)	1

Table 23. Variation in FOV for each Scenario (σ_{FOV})

Change in lesion size was considered as a variable by imaging lesions 1 cm, 2 cm, and 3 cm in diameter for each patient size, as shown in Figure 6. The standard deviation resulting from lesion size for each scenario, σ_{LESION}, was calculated in the Bayesian Hierarchical model and is shown in Table 24.

Scenario	Lesion size	Small Phantom		Medium Phantom		Large Phantom	
		95% CI for variation (σ_{LESION})	Posterior probability	95% CI for variation (σ_{LESION})	Posterior probability	95% CI for variation (σ_{LESION})	Posterior probability
III	1 cm	(-2.125, 0.857)	0.197	(-2.301, 0.773)	0.154	(-5.191, 0.824)	0.074
	2 cm	--	--	--	--	--	--
	3 cm	(-0.391, 2.477)	0.928	(-0.726, 2.099)	0.849	(-2.489, 3.120)	0.587
IV - V	1 cm	(-4.0766, 1.0409)	0.127	(-6.758, 0.024)	0.026	(-4.903, 1.393)	0.138
	2 cm	--	--	--	--	--	--
	3 cm	(-0.667, 4.237)	0.922	(-0.986, 5.909)	0.921	(-1.558, 4.157)	0.828

Table 24. Variation resulting from lesion size for scenarios where enhancement was

simulated (σ_{LESION})

The standard deviation attributed to changing lesion size, σ_{LESION}, was computed for the 1 cm and 3 cm lesions relative to the deviation of each from measurements in the 2 cm sphere. Significant differences between VUE and TUE enhancement measurements (posterior probability > 0.95 or posterior probability < 0.05) for the 1 cm sphere could be a result of partial volume averaging because the image thickness used throughout the study was 5 mm. Notice that the most change due to lesion size was observed in scenarios I and II, and could be attributable to the large differences in baselines values (-100 for scenario I and 0 for scenario II) considered in the model.

4.2.5 Discussion: Sub Aim 2.3

For discussion of the results of the phantom study, the enhancement values of interest will be labeled as follows:

$$\boldsymbol{VUE\ image\ based\ enhancement}: \Delta VUE = DECT_{post-contrast} - VUE$$

$$\boldsymbol{TUE\ image\ based\ enhancement}: \Delta TUE = SECT_{post-contrast} - TUE$$

It has been stated that the determination of enhancement is the most important criterion used to distinguish surgical from nonsurgical renal masses [17]. Based on the calculated difference between pre- and post-contrast images, a lesion is placed into one of the following categories [17]:

- Unenhancing: difference is < 10
- Indeterminate (and needs further evaluation): difference is between 10 -20 HU
- Enhancing: difference is > 20 HU

In light of this it is clear that accurate quantification of enhancement is crucial for borderline lesions, in the range of approximately 5-25 HU (when considering systematic and random error), for appropriate diagnosis of renal lesions. Considering the results of Scenarios 3 and 4 in the phantom study, it is clear that VUE as the baseline image for enhancement measurement is not a

suitable replacement for TUE images. As demonstrated in Figures 30-31 there were cases in which VUE-based enhancement measurements would have led to different categorization of the simulated lesions than TUE-based enhancement measurements. Because enhancement was always lower for VUE-based measurements, this led to categorization of "unenhancing" in many cases where the TUE-based measurements would have led to categorization of an "enhancing" or "indeterminate" lesion (requiring surgical resection or further evaluation). The clinical implications of these differences in enhancement values could be severe and lead to false negative diagnosis of renal lesions. Table 25 quantifies the number of times that VUE-based enhancement measurements lead to different categorization than TUE-based measurements for Scenarios III-V. As previously stated, the categories were considered to be unenhancing (HU < 10), intermediate (10 < HU > 20), or enhancing (HU > 20).

	Total	Scenario III	Scenarios IV-V
Number of samples	650	288	362
Number of times categorization did not match	373	229	144
Number of times categorization did match	277	59	218
Accuracy (%)	42.6%	20.5%	60.2%

Table 25. Comparison of categorization of TUE and VUE measurements to evaluate clinical relevance of the results

The percentage of matching categorization is higher for Scenarios IV-V because this includes data from Scenario V, which simulated a highly enhancing renal lesion (approximately 40 HU enhancement). Although differences between enhancement measurements were significant in Scenario V, they rarely led to differences in *categorization* of the lesion as enhancing or non-enhancing. For example, a difference of 10 HU in enhancement between TUE- and VUE-based

data for a borderline lesion enhancing 20 HU is more clinically meaningful than the same difference for a lesion that enhances a total of 50 HU. This experiment has demonstrated that for highly enhancing renal lesions, enhancement calculations for TUE and VUE images would lead to the same categorization of the lesion, and therefore confirm that VUE images would be a feasible replacement to TUE images in these cases. However, the results of scenario III-IV indicate that enhancement differences between VUE-based compared to TUE-based measurements are too significant; therefore the results of this study indicate that it is not feasible to replace TUE with VUE images in lesions which contain low concentrations of iodine in post-contrast imaging. Recall that multiphase renal CT exams are performed to characterize and diagnose renal lesions, the nature of which is not known prior to examination. As a result, VUE images are not a suitable replacement for TUE images for determination of enhancement because the feasibility could not be demonstrated in the cases of all lesion types studied in these experiments.

The presets that returned results that matched most closely to TUE based enhancement measurements were determined for each scenario by the Bayesian Hierarchical model, which quantified and accounted for sources in uncertainty resulting from the many parameters in the experiment. A summary of these results for all scenarios can be found in Table 30 in Appendix 6.6. For the small phantom GSI-29 most closely matched TUE measurements and for the medium phantom GSI-10 most closely matched. For the large phantom the protocol most closely matching TUE measurements varied for each scenario.

A note should also be made regarding the subtraction artifact, which was also observed in the retrospective study and discussed in section 4.1.4. A delrin rod with a CT number of approximately 300 HU was included in the phantom design to simulate spine. A subset of images was randomly selected for ROI measurements in the spinal region, the dimensions of which are given in Table 7. Figure 33 shows a comparison of each GSI preset to the TUE CT number measurement.
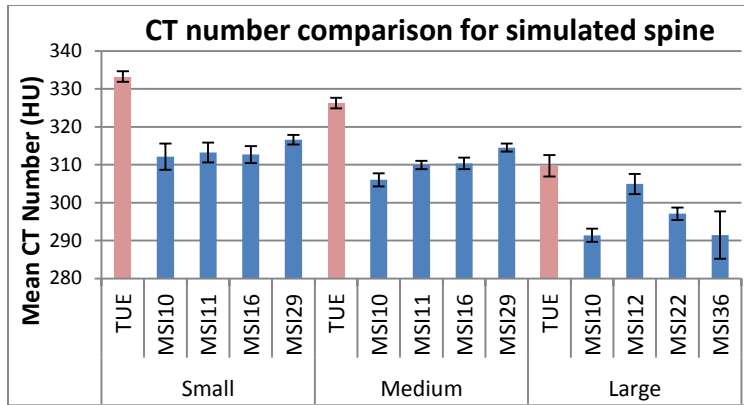
Figure 33. Comparison of VUE to TUE CT numbers measured in the delrin rod, which simulated bone.

For all measurements, the CT number measured in the VUE images was less than that measured in the TUE image. This further confirms the presence of the subtraction artifact in images reconstructed using the MSI algorithm. This is explained by the representation of all materials within each voxel as a weighted combination of water and iodine. As demonstrated in Figure 1 (section 1.3), the algorithm interprets bone as a weighted combination of water and iodine, and therefore removes the calculated fraction of iodine present resulting in removal of calcium signal in the reconstructed VUE image.

Measurements of the phantom background were recorded in a subset of images to compare the CT number in TUE to VUE images. As shown in Figure 34, the average measurements made in the phantom background are similar for TUE and VUE images, which is expected because these high density polyethylene regions did not contain iodine contrast.
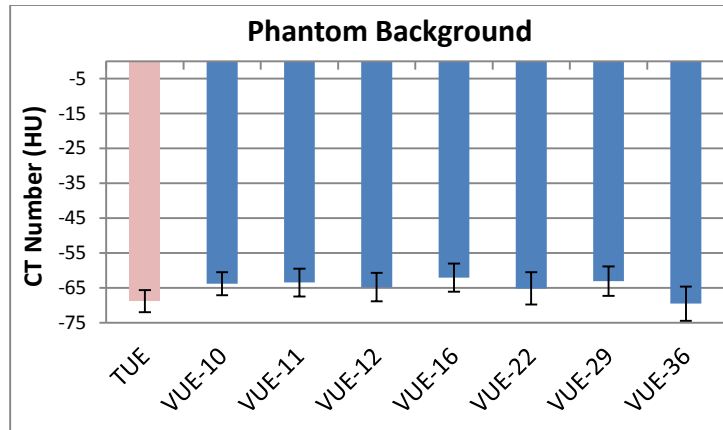
Figure 34. Comparison of each GSI preset to the average TUE CT number measured in the background of the phantom

Limitations of this study:

The MSI algorithm has been stated to replace the estimated volume of iodine with an equivalent volume of blood [27]. In light of this, use of blood for TUE baseline image acquisition, and then use of blood and Optiray mixtures would have been the most preferable experimental approach. However, due to limitations regarding the accessibility of blood, a surrogate material was used in instead of blood. The surrogate material selected was apple juice, due to the similarities in attenuation measurements and effective atomic numbers. The use of this surrogate in place of blood could have affected the results, and therefore this limitation should be considered with the results.

The phantom background is HDPE (approximately -65 HU), which has a spectral curve which varies from that of soft tissue, which potentially affected DECT measurements. The Jaszscak phantom study verified that this variation is minimally significant for VUE CT number measurements (Figures 22-23), but it was signification for DECT measurements. Consequently, the use of HDPE as the background material could have affected DECT post-contrast measurements, which would have in turn affected enhancement measurements.

Previous studies have sought to identify the optimal monochromatic keV to match 120 kVp SECT images [45]. Some preliminary results have indicated that this value may be 68 keV instead of the commonly used 70 keV. Using 70 keV for comparison to 120 kVp SECT images therefore may not be the most accurate comparison, which could affect the post-contrast measurements and consequently overall enhancement. This was assessed by measuring CT numbers for varying monochromatic energies to estimate the potential difference that could result if the 70 keV used in these experiments is not the optimal monochromatic energy for post-contrast images. An example of the difference for Scenarios III (intermediate enhancement) and IV (low enhancement) is shown in Table 26. The difference between the potentially more suitable 68 keV and the currently used 70 keV is approximately 1 HU for each case considered. Referring to Figures 30-31 (visually) and Tables 21-22 (quantitatively), the difference in enhancement is larger than 1 HU, confirming that the most considerable difference originates from VUE image measurements, and not from the selection of monochromatic energy for DECT post-contrast measurements. Selection of keV to represent 120 kVp images did not affect the results of the experiment.

keV	CT number Scenario III low enhancement (HU)	SD	CT number Scenario IV intermediate enhancement (HU)	SD
65	39.6	2.9	54.9	3.0
68	37.1	3.0	53.1	3.1
69	36.4	3.1	52.5	3.2
70	35.9	3.1	52.0	3.2
71	35.4	3.1	51.7	3.3
72	34.5	3.2	51.0	3.4
75	33.1	3.3	49.8	3.5

Table 26. Assessment of the effect of variation in monochromatic energy selection (keV) on

CT number for the small phantom using GSI protocol 29

4.3 Specific Aim 3

4.3.1 Results

Preliminary data for evaluation of the effect of ASIR level on CT number accuracy were collected in Sub Aim 2.2. The purpose for collecting this data was to compare the TUE method (60% ASIR with a soft filter) to the VUE method (0% ASIR with a standard filter) of image reconstruction in the retrospective study to determine which method to use in Sub Aim 2.3. The results of this study are shown in Table 27 and Figure 35.

ROI Section	0% ASIR Standard filter		60% ASIR Soft filter		% Difference between mean CT numbers
	Mean CT Number	Mean Noise	Mean CT Number	Mean Noise	
3 cm sphere insert	13.33	6.17	13.03	6.14	0.23
1 cm sphere insert	21.94	7.76	22.08	7.69	0.64
Spine (Delrin rod)	311.34	5.80	311.48	5.53	0.05
Phantom background	-64.75	6.41	-64.66	5.79	0.14

Table 27. Comparison of retrospective study image reconstruction techniques
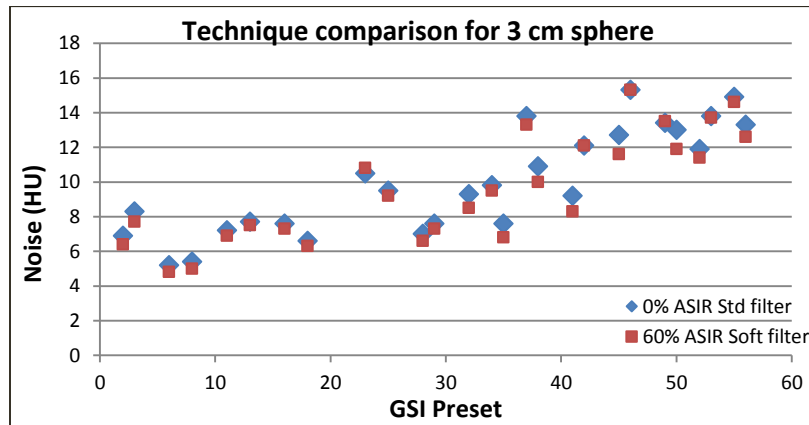
Figure 35. Comparison of retrospective study image reconstruction techniques

For Specific Aim 3, three levels of ASIR 0%, 60%, and 100% were chosen to assess the effect of ASIR level on enhancement values. Subsets of experiments from Specific Aim 2.3 were

chosen for reconstruction with the stated levels of ASIR. The results were fitted and analyzed

using a Bayesian Hierarchical model, the results of which are given in Table 28. The mean of the

slopes of ASIR level in relation to CT number for each phantom configuration is given as μ_{ASIR},

and the associated standard deviation, is given by σ_{ASIR}. A slope approaching zero implies no

difference in CT number for changing ASIR level. The absolute value of the slope indicates the

most anticipated difference in CT number resulting from maximum possible difference in ASIR

level. For example a slope of -0.0168 implies that the maximum possible difference would be

1.68 HU.

		Mean	SD	95% Confidence Interval
Small Patient	μ_{ASIR}	-0.0168	0.0042	(-0.0252, -0.0084)
	σ_{ASIR}	0.0161	0.003	(0.0113, 0.023)
Medium Patient	μ_{ASIR}	-0.0174	0.0053	(-0.0278, -0.007)
	σ_{ASIR}	0.0201	0.0039	(0.0137, 0.029)
Large Patient	μ_{ASIR}	-0.0258	0.0068	(-0.0394, -0.0126)
	σ_{ASIR}	0.0252	0.0053	(0.0166, 0.0372)

Table 28. Specific Aim 3 results

4.3.2 Discussion

Results of Sub Aim 3 indicate that there is no clinical significance resulting from

changing the level of ASIR applied to the reconstructed image on measured CT number. The

largest mean slope was -0.0258 for the large patient, which corresponds to a maximum

anticipated difference in CT number of 2.58 HU for any range of variation in ASIR level applied.

These results confirm the validity of the results from the quantitative retrospective study in

Specific Aim 1, despite the differences in reconstruction techniques. However, confirmation that

ASIR level does not quantitatively effect CT number does not validate the results of the

qualitative study. ASIR level affects the perceived "graininess" or noise of the image, and

therefore very likely had an effect on the qualitative scores given by the radiologists for VUE

images (which had 0% ASIR) as compared to TUE images (which had 60% ASIR).
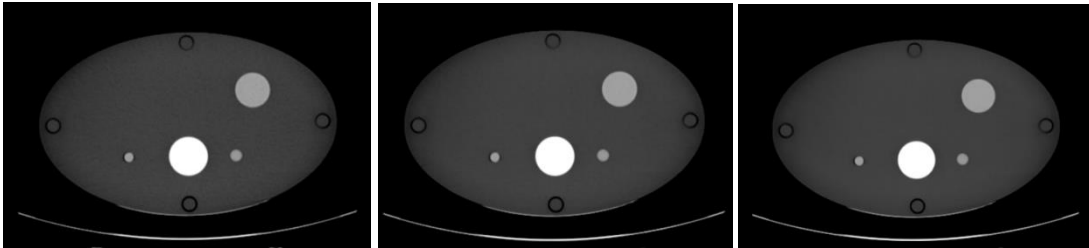
Figure 36. Visual comparison of variation in ASIR level: 0% (left), 60% (center), 100%

(right)

Chapter 5. Conclusions

5.1 Specific Aim Conclusions

The results of the retrospective study indicate that VUE images have the potential to replace TUE images clinically. In the qualitative study VUE images were found to be inferior to TUE images for visualization of major vessels and depiction of liver parenchyma, which may be attributed in part to the variation in reconstruction techniques. In the quantitative study VUE images were found to be non-inferior to TUE images only in the liver, medulla, and cystic lesions based on a paired t-test. However, after consideration of the clinical relevance of the results, VUE images were determined to be non-inferior for the spleen and subcutaneous fat as well. An important artifact observed in this study, referred to as the subtraction artifact, also affects the feasibility of replacing TUE with VUE images because of the importance of the visibility of calcifications in renal lesion characterization.

A phantom study was conducted to assess VUE images across a wide range of clinical scenarios. The results indicate that enhancement values for VUE based measurements are not significantly different from TUE based measurements for simulated AML lesions and benign cystic lesions. However, the results for simulation of Bosniak category II-IV lesions indicated that enhancement values are significantly different when using VUE as the baseline for enhancement measurements. These results indicate that for borderline enhancing lesions VUE images are not a suitable replacement for TUE images. Considering the purpose of diagnostic renal CT, in which the lesion type is not known prior to imaging, VUE images are currently not suitable for diagnosis of an unknown renal lesion type. Although the VUE images reconstructed using the MSI algorithm in its current form likely cannot be used as a replacement for TUE images, we believe the results of this study still prove the potential for this application.

The impact of ASIR level on VUE enhancement accuracy was assessed in Specific Aim 3. The results from the mixed effects model indicate that the level of ASIR applied does not affect measured CT numbers or enhancement. These results further validate the results of the quantitate study in Specific Aim 1, despite the difference in reconstruction techniques between TUE and VUE images.

5.2 Future Work

Repeating a qualitative retrospective study with radiologists (Sub Aim 1.1) where the reconstruction techniques between TUE and VUE images are identical would be valuable. Preferably, these cases would involve more renal disease, since most cases used in this retrospective analysis were patients with pancreatic indication and no associated renal lesions. Additionally, a subset of images would be selected randomly for separate qualitative evaluation of visualization of calcifications. For this study, TUE and VUE images would be shown side by side, and the radiologists would compare intensity and number of calcifications visible in each image.

Selecting a subset of experiments from Sub Aim 2.3, such as scenarios III-IV for repeated analysis with blood used would allow for more direct evaluation of the clinical performance of the algorithm.

6. Appendix

6.1 Qualitative Questionnaire

<u>Instructions</u>: An image will be presented to you, which you can window/level to your preference. Please choose one answer for each of the following questions to reflect your opinions as accurately as possible for each image given.

Number of years of experience reading CT abdominal exams: _____

<u>Survey</u>

1. Visualization of major vessels (considering hepatic, portal, and renal veins in particular)
   1. Very poor
   2. Poor
   3. Adequate
   4. Good
   5. Very good
2. Visually sharp reproduction of the pancreatic contour
   1. Very poor
   2. Poor
   3. Adequate
   4. Good
   5. Very good
3. Visualization of calcifications
   1. Very poor
   2. Poor
   3. Adequate
   4. Good
   5. Very good
4. Depiction of liver parenchyma, e.g., ability to determination of the degree of fatty infiltration
   1. Very poor
   2. Poor
   3. Adequate
   4. Good
   5. Very good
5. Visualization of adrenal glands
   1. Very poor
   2. Poor
   3. Adequate
   4. Good
   5. Very good
6. Corticomedullary differentiation
   1. No differentiation
   2. Slight differentiation
   3. Extreme differentiation

6.2 Designs for each phantom

Small Phantom Design

Small patient (5th percentile PeopleSize 2008)

= sphere
= cylinder

PMMA sphere x 3 Ø = 1.0, 2.0, 3.0 cm

6.15 cm

Delrin rod Ø = 3.67 cm

45° 3.05 cm 8.7 cm

4.5 cm

5.6 cm

PMMA sphere Ø = 1.0 cm

PMMA cylinder Ø = 1.0 cm

Medium Phantom Design

Medium patient (50th percentile PeopleSize 2008)

= sphere
= cylinder

PMMA sphere x 3 Ø = 1.0, 2.0, 3.0 cm

7.85 cm

Delrin rod Ø = 3.67 cm

45° 3.85 cm 11.1 cm

5.8 cm

7.1 cm

PMMA sphere Ø = 1.0 cm

PMMA cylinder Ø = 1.0 cm

Large Phantom Design

Large patient (95th percentile PeopleSize 2008)

Delrin rod Ø = 3.67 cm

PMMA sphere x 3 Ø = 1.0, 2.0, 3.0 cm

10.4 cm

5.1 cm 14.7 cm

45°

7.7 cm 7.7 cm

9.4 cm

PMMA sphere Ø = 1.0 cm

PMMA cylinder Ø = 1.0 cm
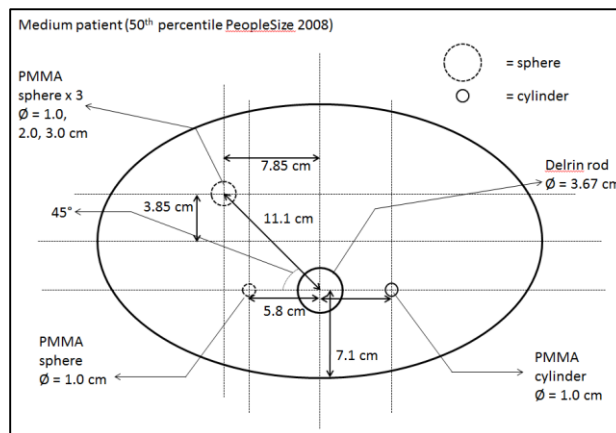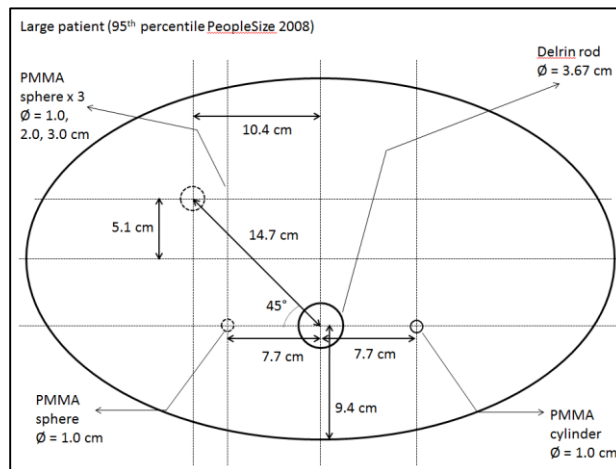
6.3 Complete List of GSI Protocols used in Sub Aim 2.2.

GSI Preset	SFOV	Rot time (s)	Beam width (mm)	mA	CTDI$_w$ (mGy)	CTDI$_{vol}$ 0.531 pitch	CTDI$_{vol}$ 0.984 pitch
1	Large	0.5	40	630	17.49	32.94	17.77
51	Large	0.5	40	260	10.18	19.17	10.35
54	Large	0.6	40	275	8.96	16.87	9.11
15	Large	0.6	40	640	21.5	40.49	21.85
31	Large	0.6	40	375	12.72	23.95	12.93
40	Large	0.6	40	360	12.09	22.77	12.29
22	Large	0.7	40	375	14.79	27.85	15.03
44	Large	0.7	40	275	10.51	19.79	10.68
48	Large	0.7	40	260	8.91	16.78	9.05
10	Large	0.8	40	600	25.13	47.33	25.54
27	Large	0.8	40	550	23.19	43.67	23.57
36	Large	0.8	40	360	10.14	19.10	10.30
4	Large	0.9	40	600	28.47	53.62	28.93
5	Large	1.0	40	600	32.01	60.28	32.53
17	Large	0.6	20	640	23.41	44.09	23.79
33	Large	0.6	20	375	13.69	25.78	13.91
24	Large	0.7	20	375	15.87	29.89	16.13
12	Large	0.8	20	600	27.33	51.47	27.77
7	Large	1.0	20	600	34.87	65.67	35.44
3	Medium	0.5	40	630	18.33	34.52	18.63
52	Medium	0.5	40	360	10.59	19.94	10.76
16	Medium	0.6	40	640	22.46	42.30	22.83
32	Medium	0.6	40	375	13.61	25.63	13.83
41	Medium	0.6	40	360	12.86	24.22	13.07
55	Medium	0.6	40	375	9.51	17.91	9.66
23	Medium	0.7	40	375	15.56	29.30	15.81
45	Medium	0.7	40	375	11.1	20.90	11.28
49	Medium	0.7	40	260	9.54	17.97	9.70
11	Medium	0.8	40	600	26.27	49.47	26.70
28	Medium	0.8	40	550	24.6	46.33	25.00
37	Medium	0.8	40	260	10.81	20.36	10.99
6	Medium	1.0	40	600	33.43	62.96	33.97

35	Medium	0.5	20	630	19.85	37.38	20.17
53	Medium	0.5	20	360	11.51	21.68	11.70
18	Medium	0.6	20	640	24.42	45.99	24.82
34	Medium	0.6	20	375	14.16	26.67	14.39
42	Medium	0.6	20	360	14.07	26.50	14.30
56	Medium	0.6	20	275	10.34	19.47	10.51
25	Medium	0.7	20	375	16.76	31.56	17.03
46	Medium	0.7	20	275	11.99	22.58	12.18
50	Medium	0.7	20	260	10.24	19.28	10.41
13	Medium	0.8	20	600	28.58	53.82	29.04
29	Medium	0.8	20	550	26.74	50.36	27.17
38	Medium	0.8	20	260	11.69	22.02	11.88
2	Medium	0.9	20	600	32.32	60.87	32.85
8	Medium	1.0	20	600	36.34	68.44	36.93

6.4 Phantom study image acquisition matrix examples

Patient Size	Lesion Size	Image	Patient Size	Lesion Size	Image	Patient Size	Lesion Size	Image
Small	1 cm	TUE	Medium	1 cm	TUE	Large	1 cm	TUE
		Post-contrast			Post-contrast			Post-contrast
	2 cm	TUE		2 cm	TUE		2 cm	TUE
		Post-contrast			Post-contrast			Post-contrast
	3 cm	TUE		3 cm	TUE		3 cm	TUE
		Post-contrast			Post-contrast			Post-contrast

Table 29. SECT image acquisition checklist for each scenario

Patient Size	Lesion Size	GSI preset	Patient Size	Lesion Size	Thickness (mm)	GSI preset	Patient Size	Lesion Size	GSI preset
SMALL	1 cm	10	MEDIUM	1 cm	5	10	Large	1 cm	10
		11				11			12
		16				16			22
		29				29			36
	2 cm	10		2 cm	5	10			10
		11				11			12
		16				16			22
		29				29			36
	3 cm	10		3 cm	5	10			10
		11				11			12
		16				16			22
		29				29			36

Table 30. DECT image acquisition checklist for each post-contrast scenario for VUE images

reconstruction

6.5 Sub Aim 1 Results: Intra-observer variability between the radiologists
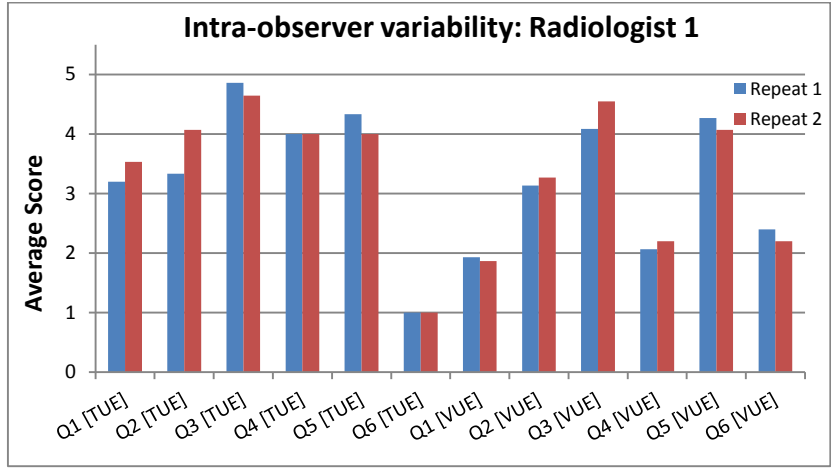
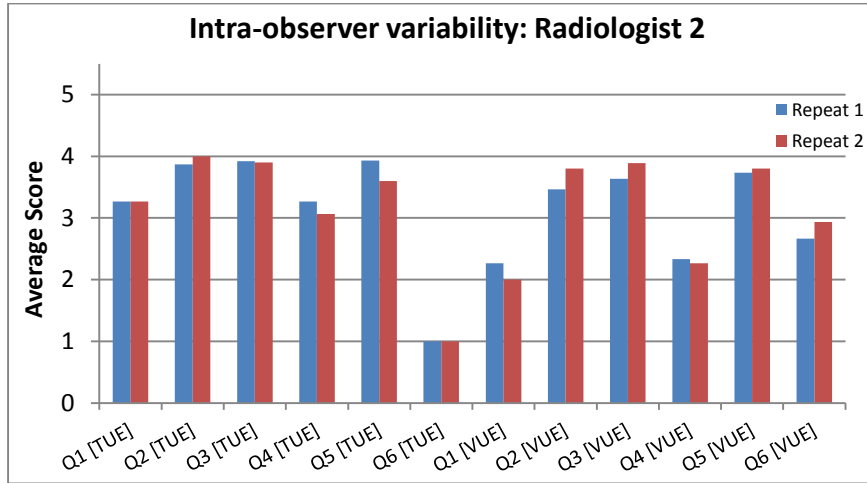

Figure 37. Intra-observer variability for Radiologist 1

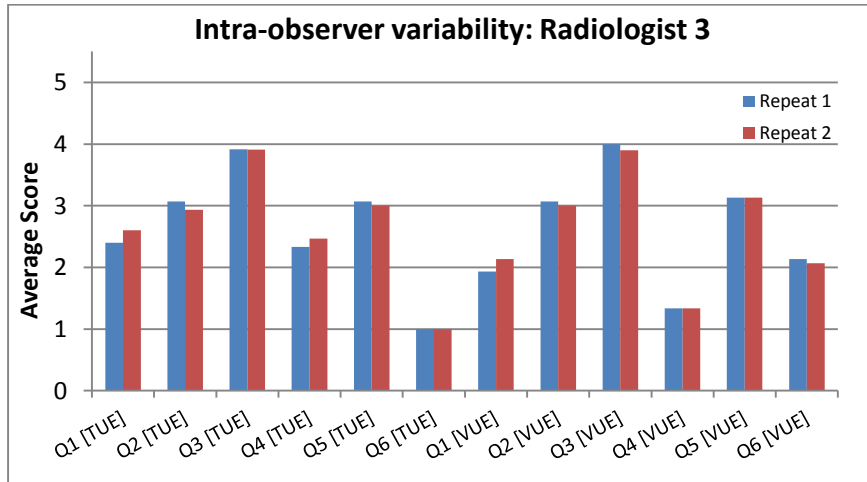**Figure 38. Intra-observer variability for Radiologist 2**

Figure 39. Intra-observer variability for Radiologist 3

6.6 Phantom Study Simulation 1 graphs

The error bars for each graph represent ± the standard deviation for the results represented by each bar in the graph.

Scenario 1

Figure 40. Comparison of TUE vs. VUE enhancement values for variation of position of lesion within the FOV for the 1 cm sphere and the specified GSI protocols.

Figure 41. Comparison of TUE vs. VUE enhancement values for variation in phantom and lesion sizes for the specified GSI protocols and lesions located in the periphery of the SFOV.

Scenario 2

Figure 42. Comparison of TUE vs. VUE enhancement values for variation in phantom size

for 2 cm lesion and the identified GSI protocols.
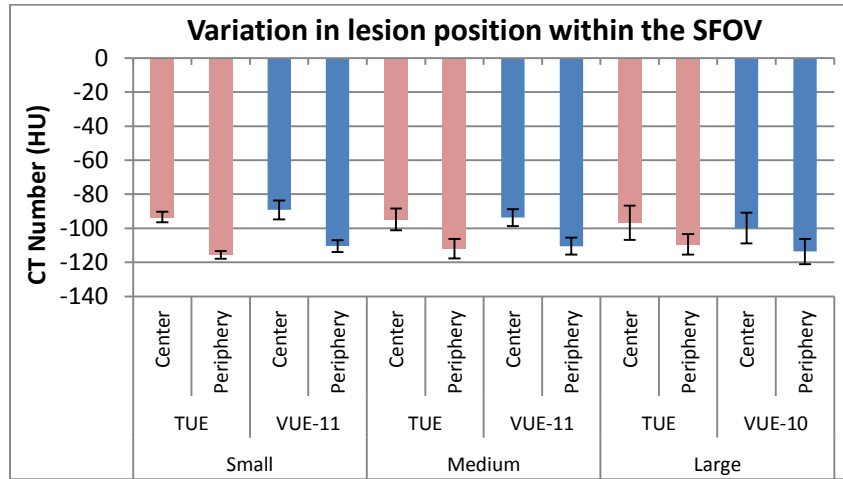
Scenario 3
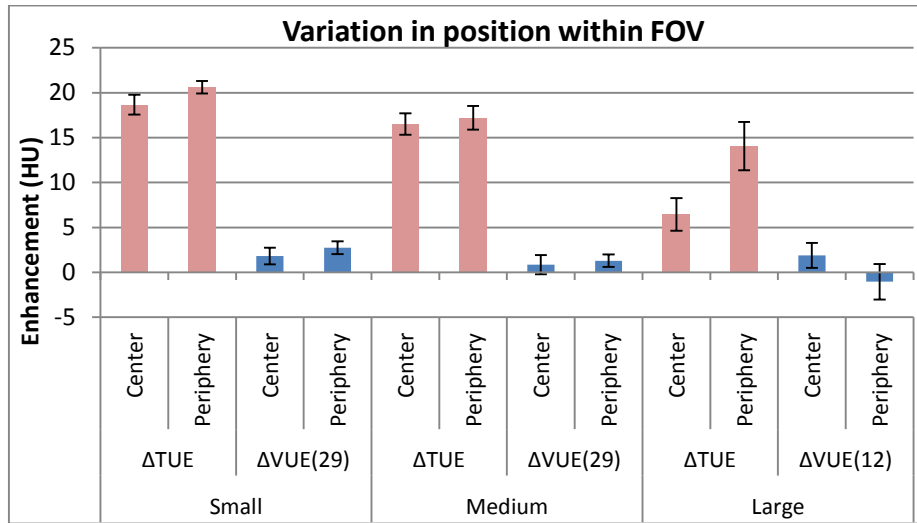
Figure 43. Comparison of TUE vs. VUE enhancement values for variation of position of

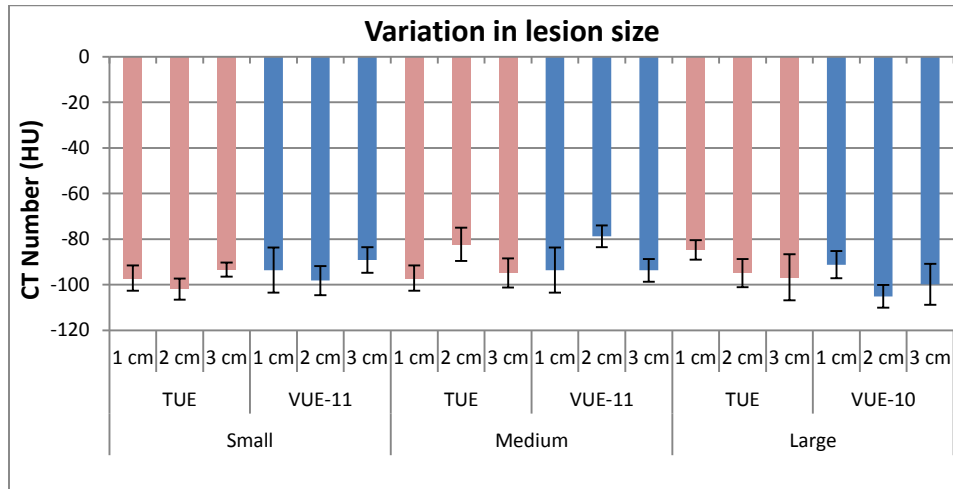**lesion within the FOV for the 1 cm sphere and the specified GSI.**

Scenario 4

Figure 44. Comparison of TUE vs. VUE enhancement values for variation in phantom and lesion sizes for the GSI protocols specified and lesions located in the periphery of the SFOV.
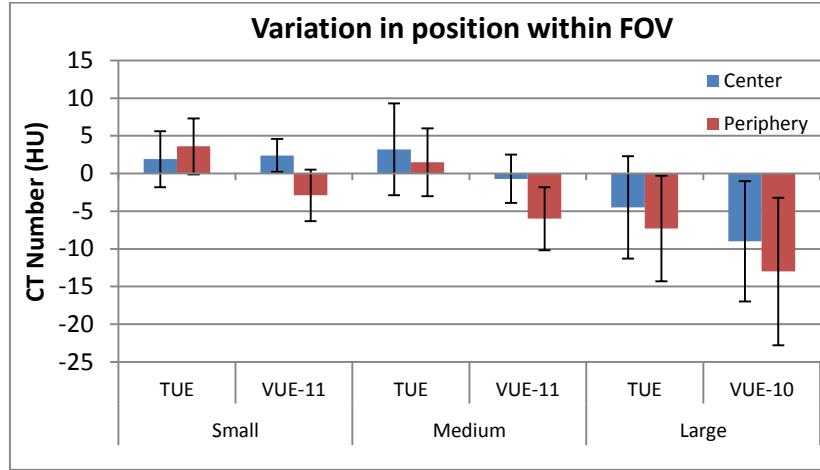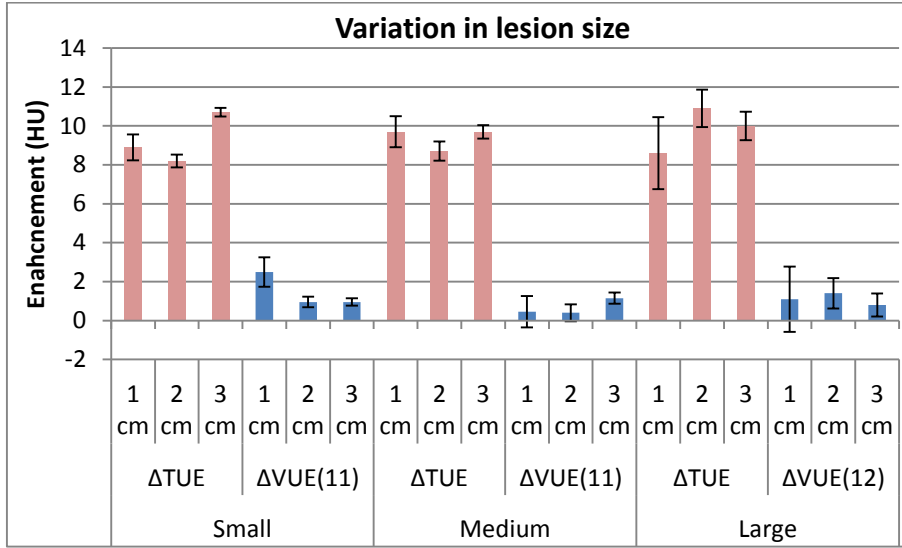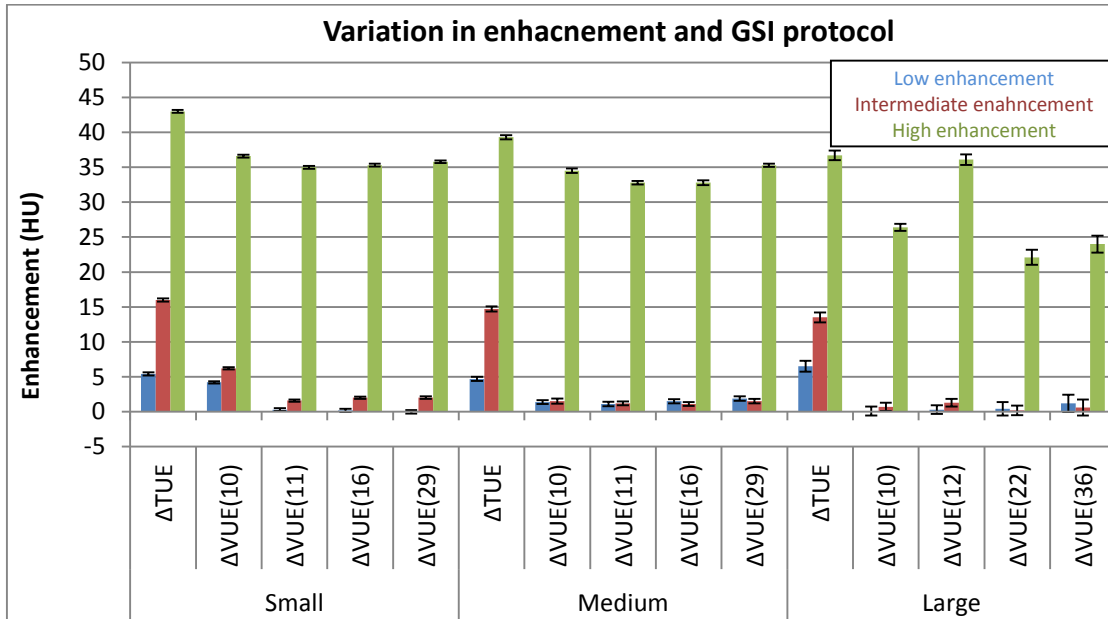
Scenario 5

Figure 45. Overall comparison of low, intermediate, and high enhancement scenarios for a 40 HU baseline for the 3 cm lesions located in the periphery of the SFOV

Scenario	Protocol	Small Phantom			Medium Phantom			Large Phantom		
		Mean	SD	Ext Val	Mean	SD	Ext Val	Mean	SD	Ext Val
I and II	β.VUE-10	0.159	0.8689	0.564	-0.0065	0.8878	0.502	-2.3863	3.2323	0.238
	β.VUE-11 (12)	0.1644	0.8742	0.555	0.0605	0.8894	0.515	-2.2122	3.0847	0.25
	β.VUE-16 (22)	0.1768	0.9766	0.56	0.2176	0.9704	0.56	-2.525	3.427	0.226
	β.VUE-29 (36)	0.0786	0.8685	0.524	0.0977	0.8711	0.531	-1.8309	2.9779	0.273
III	β.VUE-10	-16.3479	0.9537	0	-13.8417	0.858	0	-7.5158	1.4429	0
	β.VUE-11 (12)	-16.4564	0.9552	0	-14.2445	0.863	0	-6.9222	1.4306	0
	β.VUE-16 (22)	-16.5018	0.9606	0	-14.0403	0.8465	0	-8.6903	1.3984	0
	β.VUE-29 (36)	-16.2392	0.9296	0	-14.3276	0.8613	0	-7.4961	1.4352	0
IV and V	β.VUE-10	-8.1564	1.1752	0	-9.0207	1.5786	0	-9.7155	1.7239	0
	β.VUE-11 (12)	-9.722	1.2145	0	-10.1018	1.6279	0	-7.9408	1.7143	0
	β.VUE-16 (22)	-9.3679	1.2082	0	-9.4814	1.6648	0	-10.9021	1.765	0
	β.VUE-29 (36)	-9.053	1.2733	0	-8.8473	1.6781	0	-8.372	1.6895	0

Table 31. Summary of the results for differences in enhancement measurements when using VUE images (for each selected protocol) compared to TUE images as the baseline for calculation of enhancement (where the mean and SD values are for the difference in enhancement were computed in the Bayesian Hierarchical model, and are therefore not raw differences). The GSI protocol which varied least from TUE enhancement measurements for each scenario is highlighted.

7. Bibliography

1. J. T. Bushberg, J.A.S., E. M. Leidholdt Jr, J. M. Boone, *The Essential Physics of Medical Imaging*. 3rd ed. 2011, Philadelphia, Pa: Lippincott Williams and Wilkins.

2. Kalender, W.A., *X-ray computed tomography*. Physics in medicine and biology, 2006. **51**(13): p. R29.

3. Coursey, C.A., R.C. Nelson, D.T. Boll, E.K. Paulson, L.M. Ho, A.M. Neville, D. Marin, R.T. Gupta, and S.T. Schindera, *Dual-energy multidetector CT: how does it work, what can it tell us, and when can we use it in abdominopelvic imaging? 1.* Radiographics, 2010. **30**(4): p. 1037-1055.

4. Brooks, R.A. and G. Di Chiro, *Theory of Image Reconstruction in Computed Tomography 1.* Radiology, 1975. **117**(3): p. 561-572.

5. Huda, W. and R.M. Slone, *Review of radiologic physics*. 2003: Lippincott Williams & Wilkins.

6. Johnson, T.R., B. Krauss, M. Sedlmair, M. Grasruck, H. Bruder, D. Morhard, C. Fink, S. Weckbach, M. Lenhard, and B. Schmidt, *Material differentiation by dual energy CT: initial experience*. European radiology, 2007. **17**(6): p. 1510-1517.

7. Marin, D., D.T. Boll, A. Mileto, and R.C. Nelson, *State of the Art: Dual-Energy CT of the Abdomen.* Radiology, 2014. **271**(2): p. 327-342.

8. N. Chandra, D.A.L., T. R. C. Johnson, *Gemstone Detector: Dual Energy Imaging via Fast kVp Switching*, in *Dual Energy CT in Clinical Practice*. 2011, Medical Radiology. p. 35-41.

9. Graser, A., T.R. Johnson, E.M. Hecht, C.R. Becker, C. Leidecker, M. Staehler, C.G. Stief, H. Hildebrandt, M.C. Godoy, and M.E. Finn, *Dual-energy ct in patients suspected of having renal masses: Can virtual nonenhanced images replace true nonenhanced images? 1.* Radiology, 2009. **252**(2): p. 433-440.

10.   Mendonça, P.R., R. Bhotika, M. Maddah, B. Thomsen, S. Dutta, P.E. Licato, and M.C. Joshi. *Multi-material decomposition of spectral CT images*. in *SPIE Medical Imaging*. 2010. International Society for Optics and Photonics.

11.   Alvarez, R.E. and A. Macovski, *Energy-selective reconstructions in x-ray computerised tomography*. Physics in medicine and biology, 1976. **21**(5): p. 733.

12.   Kalender, W.A., W. Perman, J. Vetter, and E. Klotz, *Evaluation of a prototype dual-energy computed tomographic apparatus. I. Phantom studies*. Medical physics, 1986. **13**(3): p. 334-339.

13.   Chandra, N., *Material Attenuation Coefficient* in *GE presentation*, D.E. Physics, Editor.

14.   Xu, D., D.A. Langan, X. Wu, J.D. Pack, T.M. Benson, J.E. Tkaczky, and A.M. Schmitz. *Dual energy CT via fast kVp switching spectrum estimation*. in *SPIE Medical Imaging*. 2009. International Society for Optics and Photonics.

15.   Bosniak, M.A., *Diagnosis and management of patients with complicated cystic lesions of the kidney*. AJR. American journal of roentgenology, 1997. **169**(3): p. 819-821.

16.   Bosniak, M.A., *The current radiological approach to renal cysts*. Radiology, 1986. **158**(1): p. 1-10.

17.   Israel, G.M. and M.A. Bosniak, *How I Do It: Evaluating Renal Masses 1*. Radiology, 2005. **236**(2): p. 441-450.

18.   Israel, G.M. and M.A. Bosniak, *Pitfalls in Renal Mass Evaluation and How to Avoid Them 1*. Radiographics, 2008. **28**(5): p. 1325-1338.

19.   E. Cho, H.O.A., P. Lindblad, *Epidemiology of Renal Cell Carcinoma*. Hematology/ Oncology Clinics **25**(4): p. 651-665.

20.   Institute, N.C., *SEER Stat Fact Sheets: Kidney and Renal Pelvis Cancer*, Surveillance Research Program: http://seer.cancer.gov/statfacts/html/kidrp.html.

21.   G. M. Israel, M.A.B., *An Update of the Bosniak Renal Cyst Classification System*. Urology, 2005. **66**: p. 484-488.

22.   Pooler, B.D., P.J. Pickhardt, S.D. O'Connor, R.J. Bruce, S.R. Patel, and S.Y. Nakada, *Renal cell carcinoma: attenuation values on unenhanced CT.* American Journal of Roentgenology, 2012. **198**(5): p. 1115-1120.

23.   Song, C., G.E. Min, K. Song, J.K. Kim, B. Hong, C.-S. Kim, and H. Ahn, *Differential diagnosis of complex cystic renal mass using multiphase computerized tomography.* The Journal of urology, 2009. **181**(6): p. 2446-2450.

24.   Macari, M. and M.A. Bosniak, *Delayed CT to Evaluate Renal Masses Incidentally Discovered at Contrast-enhanced CT: Demonstration of Vascularity with Deenhancement 1.* Radiology, 1999. **213**(3): p. 674-680.

25.   J. K. Kim, S.Y.P., J. H. Shon, K. S. Cho, *Angiomyolipoma with Minimal Fat: Differentiation from Renal Cell Carcinoma at Biphasic Helical CT.* Radiology, 2004. **230**: p. 677-684.

26.   C. W. Yang, S.H.S., Y. H. Chang, H. J. Chung, J. H. Wang, A. TL. Lin, K. K. Chen, *Are there useful CT features to Differentiate Renal Cell Carcinoma from Lipid-Poor Renal Angiomyolipoma?* AJR. American journal of roentgenology, 2013. **201**(5): p. 1017-28.

27.   Maddah, M., P.R. Mendonça, and R. Bhotika. *Physically meaningful virtual unenhanced image reconstruction from dual-energy CT.* in *Biomedical Imaging: From Nano to Macro, 2010 IEEE International Symposium on.* 2010. IEEE.

28.   Song, K.D., C.K. Kim, B.K. Park, and B. Kim, *Utility of iodine overlay technique and virtual unenhanced images for the characterization of renal masses by dual-energy CT.* American Journal of Roentgenology, 2011. **197**(6): p. W1076-W1082.

29.   Barrett, T., D. Bowden, N. Shaida, E. Godfrey, A. Taylor, D. Lomas, and A. Shaw, *Virtual unenhanced second generation dual-source CT of the liver: is it time to discard the conventional unenhanced phase?* European journal of radiology, 2012. **81**(7): p. 1438-1445.

30. De Cecco, C.N., A. Darnell, N. Macías, J.R. Ayuso, S. Rodríguez, J. Rimola, M. Pagés, Á. García-Criado, M. Rengo, and A. Laghi, *Virtual unenhanced images of the abdomen with second-generation dual-source dual-energy computed tomography: image quality and liver lesion detection.* Investigative radiology, 2013. **48**(1): p. 1-9.

31. Moon, J., B. Park, C. Kim, and S. Park, *Evaluation of virtual unenhanced CT obtained from dual-energy CT urography for detecting urinary stones.* Evaluation, 2012. **85**(1014).

32. Takahashi, N., R.P. Hartman, T.J. Vrtiska, A. Kawashima, A.N. Primak, O.P. Dzyubak, J.N. Mandrekar, J.G. Fletcher, and C.H. McCollough, *Dual-energy CT iodine-subtraction virtual unenhanced technique to detect urinary stones in an iodine-filled collecting system: a phantom study.* AJR. American journal of roentgenology, 2008. **190**(5): p. 1169.

33. Sommer, C.M., C.B. Schwarzwaelder, W. Stiller, S.T. Schindera, U. Stampfl, N. Bellemann, M. Holzschuh, J. Schmidt, J. Weitz, and L. Grenacher, *Iodine removal in intravenous dual-energy CT-cholangiography: Is virtual non-enhanced imaging effective to replace true non-enhanced imaging?* European journal of radiology, 2012. **81**(4): p. 692-699.

34. Pache, G., B. Krauss, P. Strohm, U. Saueressig, P. Blanke, S. Bulla, O. Schäfer, P. Helwig, E. Kotter, and M. Langer, *Dual-Energy CT Virtual Noncalcium Technique: Detecting Posttraumatic Bone Marrow Lesions—Feasibility Study 1.* Radiology, 2010. **256**(2): p. 617-624.

35. Reagan, A.C., P.I. Mallinson, T. O'Connell, P.D. McLaughlin, B. Krauss, P.L. Munk, S. Nicolaou, and H.A. Ouellette, *Dual-Energy Computed Tomographic Virtual Noncalcium Algorithm for Detection of Bone Marrow Edema in Acute Fractures: Early Experiences.* Journal of computer assisted tomography, 2014.

36. Yamada, S., T. Ueguchi, T. Ogata, H. Mizuno, R. Ogihara, M. Koizumi, T. Shimazu, K. Murase, and K. Ogawa, *Radiotherapy treatment planning with contrast-enhanced*

computed tomography: feasibility of dual-energy virtual unenhanced imaging for improved dose calculations. Radiation Oncology, 2014. **9**(1): p. 1-10.

37.   Graser, A., C.R. Becker, M. Staehler, D.A. Clevert, M. Macari, N. Arndt, K. Nikolaou, W. Sommer, C. Stief, and M.F. Reiser, *Single-phase dual-energy CT allows for characterization of renal masses as benign or malignant.* Investigative radiology, 2010. **45**(7): p. 399-405.

38.   L. Wang, B.L., X. Wu, J. Wang. Y. Zhou, W. Wang, X. Zhu, Y. Yu. X. Li, S. Zhang, Y. Shen, *Correlation between CT attenuation value and iodine concentration in vitro: Discrepancy between gemstone spectral imaging on single-source dual-energy CT and traditional polychromatic X-ray imaging.* Journal of Medical Imaging and Radiation Oncology, 2012. **56**: p. 379-383.

39.   A. Jonisch, A.N.R., P. G. Mutalik, G. M. Israel, *Can High-Attenuation Renal Cysts be Differentiated from Renal Cell Carcinoma at Unehanced CT?* Radiology, 2007. **243**(2): p. 445-450.

40.   R. Vikram, C.S.N., P. Tamboli, N. M. Tannir, E. Jonasch, S. F. Matin, C. G. Wood, C. M. Sandler, *Papillary Renal Cell Carcinoma: Radiologic-Pathologic Correlation and Spectrum of Disease.* RadioGraphics, 2009. **29**: p. 741-757.

41.   Taylor, J.R., *An Introduction to Error Analysis: the study of uncertainties in physical measurements*. Second Edition ed. 1982: Maple-Vail book manufacturing group.

42.   Viera, A.J. and J.M. Garrett, *Understanding interobserver agreement: the kappa statistic.* Fam Med, 2005. **37**(5): p. 360-363.

43.   Toepker, M., T. Moritz, B. Krauss, M. Weber, G. Euller, T. Mang, F. Wolf, C.J. Herold, and H. Ringl, *Virtual non-contrast in second-generation, dual-energy computed tomography: reliability of attenuation values.* European journal of radiology, 2012. **81**(3): p. e398-e405.

44.   D. Zhang, X.L., B. Liu, *Objective characterization of GE Discovery CT750 HD scanner: Gemstone spectral imaging mode.* Med Phys, 2011. **38**: p. 1178-1188.

45.   M. Goodsitt, E.G.C., S. C. Larson, *Accuracies of the synthesized monochromatic CT numbers and effective atomic numbers obtained with a rapid kV switching dual energy CT scanner.* Med Phys, 2011. **38**(4): p. 2222-2232.

8. Vita

Dawn Olivia Popnoe was born in New Port Richey, Florida on May 10, 1991, the daughter of Mark Thomas Skeen and Victoria Marie Skeen. After graduating Valedictorian of Okeechobee High School, Okeechobee, Florida in 2009 she entered Angelo State University in San Angelo, Texas. She received Bachelor of Science degrees with a major in Physics and a major in Mathematics. In August of 2013 she entered the Medical Physics Master's program at The University of Texas Graduate School of Biomedical Sciences at Houston. After graduation, Olivia plans to continue her education by pursing a Doctorate of Medical Physics at the University of Texas Health and Science Center in San Antonio, Texas.

Permanent Address:

608 N 23rd St
Lamesa, Tx 79331